ACKNOWLEDGMENTS

We thank M. Sawaya and M. Collazo for their assistance with crystallography, conducted at the UCLA-DOE X-ray Crystallization and Crystallography Core Facilities, which are supported by DOE grant DE-FC02-02ER63421. We thank M. Capel, K. Rajashankar, N. Sukumar, J. Schuermann, I. Kourinov, and F. Murphy at Northeastern Collaborative Access Team beamlines 24-ID-E and 24-ID-C at the Advanced Photon Source (APS), which are supported by grants from the National Center for Research Resources (5P41RR015301-10) and the National Institute of General Medical Sciences (8 P41 GM103403-10) of the National Institutes of Health. Use of the APS is supported by DOE under contract no. DE-AC02-06CH11357. We thank the staff at the Advanced Light Source SIBYLS beamline at Lawrence Berkeley National Laboratory, including K. Burnett, G. Hura, M. Hammel, J. Tanamachi, and J. Tainer for the services provided through the mail-in SAXS program, which is supported by the DOE Office of Biological and Environmental Research Integrated Diffraction Analysis program and the NIH project MINOS (Macromolecular Insights on Nucleic Acids Optimized by Scattering; grant no. RO1GM105404). We also thank U. Nattermann for help with EM, Y. Hsia for assistance with light-scattering experiments, C. Stafford for mass spectroscopy assistance, B. Nickerson for assistance with in vitro assembly experiments, and G. Rocklin for providing scripts used in data analysis. This work was supported by the Howard Hughes Medical Institute (S.G., D.C., T.G., and D.B.) and its Janelia Research Campus visitor program (S.G.), the Bill and Melinda Gates Foundation (D.B. and N.P.K.), Takeda Pharmaceutical Company (N.P.K.), NSF (grant no. CHE-1332907 to D.B. and T.O.Y.), the Air Force Office of Scientific Research (grant no. FA950-12-10112 to D.B.), and the Defense Advanced Research Projects Agency (grant no. W911NF-14-1-0162 to D.B. and N.P.K.). Y.L. was supported by a Whitcome Fellowship through the UCLA Molecular Biology Institute, and J.B.B. was supported by a NSF graduate research fellowship (grant no. DGE-0718124). Coordinates and structure factors were deposited in the Protein Data Bank with accession codes 5IM5 (I53-40), 5IM4 (I52-32), and 5IM6 (I32-28). J.B.B., W.S., N.P.K., D.E., and D.B. have filed a nonprovisional U.S. patent application, no. 14/930,792, related to the work presented herein.

SUPPLEMENTARY MATERIALS

www.sciencemag.org/content/353/6297/389/suppl/DC1
Materials and Methods
Supplementary Text
Figs. S1 to S13
Tables S1 to S6
References (*38*–*60*)
Databases S1 to S3

15 April 2016; accepted 21 June 2016
10.1126/science.aaf8818

MITOCHONDRIA

Mitochondrial endonuclease G mediates breakdown of paternal mitochondria upon fertilization

Qinghua Zhou,[1]*† Haimin Li,[1]* Hanzeng Li,[1,2]* Akihisa Nakagawa,[1] Jason L. J. Lin,[3] Eui-Seung Lee,[1] Brian L. Harry,[1,4] Riley Robert Skeen-Gaar,[1] Yuji Suehiro,[5] Donna William,[6] Shohei Mitani,[5] Hanna S. Yuan,[3] Byung-Ho Kang,[7]‡ Ding Xue[1]‡

Mitochondria are inherited maternally in most animals, but the mechanisms of selective paternal mitochondrial elimination (PME) are unknown. While examining fertilization in *Caenorhabditis elegans*, we observed that paternal mitochondria rapidly lose their inner membrane integrity. CPS-6, a mitochondrial endonuclease G, serves as a paternal mitochondrial factor that is critical for PME. We found that CPS-6 relocates from the intermembrane space of paternal mitochondria to the matrix after fertilization to degrade mitochondrial DNA. It acts with maternal autophagy and proteasome machineries to promote PME. Loss of *cps-6* delays breakdown of mitochondrial inner membranes, autophagosome enclosure of paternal mitochondria, and PME. Delayed removal of paternal mitochondria causes increased embryonic lethality, demonstrating that PME is important for normal animal development. Thus, CPS-6 functions as a paternal mitochondrial degradation factor during animal development.

Mitochondria are critical for many cellular processes including cellular respiration, apoptosis, and metabolism, and they possess their own genome (mtDNA) (*1*, *2*). However, only maternal mitochondria are passed on to progeny. Although elimination of paternal mtDNA can occur at various developmental stages through different mechanisms (*3*), it is unclear why and how paternal mitochondria are selectively eliminated after fertilization during embryo development (*3*, *4*). To address these questions, we examined paternal mitochondria in *C. elegans* spermatozoa and embryos by electron microscopy (EM) and tomography.

Mitochondria in wild-type (N2) spermatozoa are spherical (fig. S1A), with an average diameter of 464 ± 68 nm (SD), and their cristae, formed by extensive infolding of the inner membrane, uniformly distribute in the matrix (Fig. 1A). Paternal mitochondria in N2 zygotes are readily distinguished from the tubular and thinner maternal mitochondria (with an average width of 238 ± 57 nm; fig. S1B). Notably, all paternal mitochondria in N2 zygotes have multiple dark aggregates (agg) in the matrix that form promptly after their entry into oocytes (Fig. 1, B and E, fig. S1, B to G, and movie S1). The double-layer membranes from autophagosomes have started to assemble around some paternal mitochondria at this stage (fig. S1B). We named paternal mitochondria containing small aggregates that lack nearby autophagosome membranes "small agg PM" (Fig. 1B). Those containing larger aggregates that are associated with autophagosome membranes are called "large agg PM" (Fig. 1C), and those with few cristae and enclosed in an autophagosome are called "ghost PM" (Fig. 1D). Many small agg PM arise independently of the autophagy machinery (Fig. 1, B and E, fig. S1, B to G, and movie S1). Large agg PM and ghost PM are observed in N2 zygotes but are mostly seen in two- or four-cell–stage embryos (Fig. 1, C to E).

In large agg PM, cristae are cleared from the central region as the aggregates enlarge in the matrix (Fig. 1C), which occurs before autophagosomes enclose paternal mitochondria. Once enclosed by autophagosomes, they lose matrix contents except for some remaining aggregates, but their outer membrane does not rupture until most of the cristae have disappeared (Fig. 1D and fig. S1H). These results suggest that paternal mitochondria are destroyed partly in embryos by self-initiated internal breakdown prior to autophagosome assembly and degradation.

To identify intrinsic mitochondrial factors involved in paternal mitochondrial elimination (PME), we performed an RNA interference (RNAi) screen against 217 *C. elegans* nuclear genes predicted to encode mitochondrial proteins (table S1), using a sensitive polymerase chain reaction (PCR)–based method and a 3053–base pair (bp) mtDNA deletion allele (*uaDf5*; Fig. 2A) to track the fate of mtDNA (*5*). *uaDf5* mtDNA was detected in cross-progeny at all developmental stages from mating of N2 males with *uaDf5/+* heteroplasmic hermaphrodites (fig. S2A) (*5*) but was detected only in early embryos, not in late embryos nor in larval cross-progeny from N2 hermaphrodites mated with *uaDf5/+* males (Fig. 2B); these findings indicate that PME is conserved in *C. elegans* (*5*–*7*). RNAi of the *cps-6* gene, which encodes a homolog of human mitochondrial endonuclease G (*8*, *9*), caused persistence of

[1]Department of Molecular, Cellular, and Developmental Biology, University of Colorado, Boulder, CO 80309, USA. [2]Department of Chemistry and Biochemistry, University of Colorado, Boulder, CO 80309, USA. [3]Institute of Molecular Biology, Academia Sinica, Taipei 11529, Taiwan. [4]Medical Scientist Training Program, University of Colorado, Aurora, CO 80045, USA. [5]Department of Physiology, Tokyo Women's Medical University, School of Medicine and CREST, Japan Science and Technology Agency, Tokyo 162-8666, Japan. [6]Department of Microbiology and Cell Science, University of Florida, Gainesville, FL 32611, USA. [7]School of Life Sciences, Centre for Cell and Developmental Biology and State Key Laboratory of Agrobiotechnology, Chinese University of Hong Kong, Hong Kong, China.
*These authors contributed equally to this work. †Present address: First Affiliated Hospital, Biomedical Translational Research Institute, Jinan University, Guangzhou 510630, China. ‡**Corresponding author. Email: ding.xue@colorado.edu (D.X.); bkang@cuhk.edu.hk (B.-H.K.)**

paternal *uaDf5* mtDNA until the late stages of embryogenesis—a finding not observed in RNAi of other genes (fig. S2B and supplementary materials). A 336-bp deletion *(tm3222)* in *cps-6*, which removes the catalytic site of CPS-6 (fig. S2C) (*10*), had the same effect as *cps-6(RNAi)*, leading to persistence of paternal *uaDf5* mtDNA throughout embryo development (Fig. 2C), whereas *uaDf5* was detected only in 64-cell or earlier embryos in crosses between *uaDf5*/+ males and N2 hermaphrodites (Fig. 2B). These results indicate that *cps-6* is associated with rapid removal of paternal mtDNA during early embryogenesis.

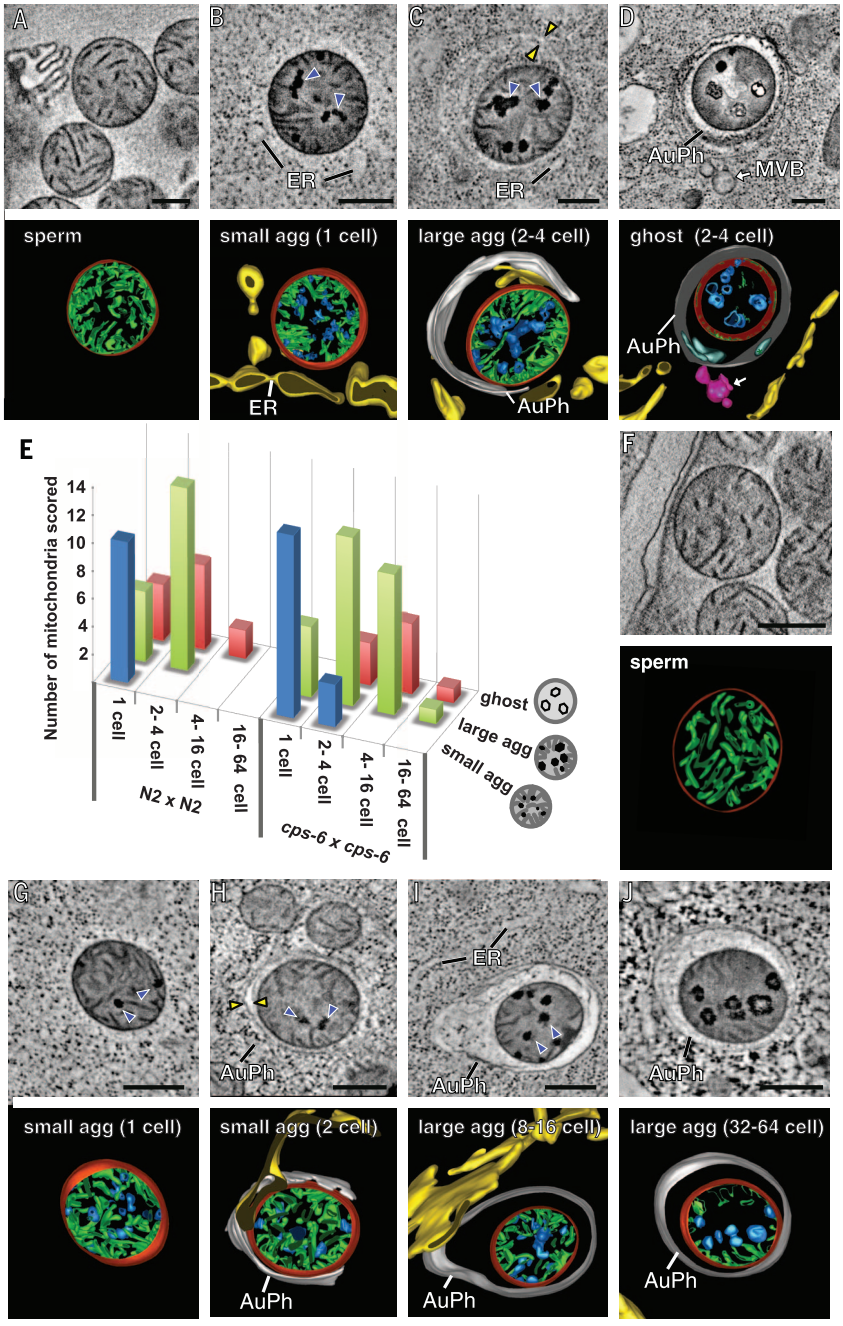

Fig. 1. Loss of *cps-6* delays internal breakdown of paternal mitochondria after fertilization. (**A** to **D**, **F** to **J**) Tomographic slice images and corresponding 3D models of a mitochondrion in an N2 (A) or *cps-6(tm3222)* (F) spermatozoon or a paternal mitochondrion in an N2 embryo [(B) to (D)] or a *cps-6(tm3222)* embryo [(G) to (J)] at the indicated stages. 3D models of autophagosomes (AuPh) and endoplasmic reticulum (ER) are shown. Mitochondrial membranes, cristae, and aggregates are colored red, green, and blue, respectively. Dark aggregates and autophagosome membranes are indicated with blue and yellow arrowheads, respectively. Scale bars, 300 nm. (**E**) Histogram showing three classes of paternal mitochondria in embryos of different stages from the indicated N2 cross (n = 45) or *cps-6(tm3222)* cross (n = 56).

We performed microscopic analysis to monitor the disappearance of paternal mitochondria stained by Mitotracker Red (MTR), a mitochondrion-specific dye (*5*). When MTR-stained N2 males were mated with unstained N2 hermaphrodites, MTR-stained paternal mitochondria were seen in embryos before the 64-cell stage (fig. S3, A to G), indicating that PME occurs in concert with paternal mtDNA elimination (Fig. 2B). Conversely, loss of *cps-6* resulted in persistence of MTR paternal mitochondria to around the 550-cell stage (fig. S3, H to N), confirming that CPS-6 promotes rapid clearance of paternal mitochondria.

CPS-6 was first identified as an apoptotic nuclease that translocates from mitochondria to the nucleus during apoptosis to mediate chromosome fragmentation (*8*, *9*). A nonapoptotic role of CPS-6 in *C. elegans* has not been reported. We used both the PCR assay and the microscopic assay to investigate whether CPS-6 is required paternally or maternally for PME (supplementary text) and found that a significant portion of paternal mitochondria and mtDNA persisted past the 64-cell stage when paternal *cps-6* was defective (Fig. 2, D and E, matings 3 and 4). By contrast, embryos without maternal *cps-6* displayed normal PME (Fig. 2, D and E, mating 2). These results indicate that paternal CPS-6 is required to promote PME.

CPS-6 is imported into mitochondria through a mitochondrial targeting sequence (amino acids 1 to 21), because CPS-6ΔN, lacking this targeting sequence, localizes to the nucleus (*8*). Expression of CPS-6, but not CPS-6ΔN, in *cps-6(tm3222)* males through the ubiquitously expressed *dpy-30* gene promoter rescued the defect in PME (Fig. 2F, matings 1, 2, and 5 to 7; see also supplementary text), indicating that localization of CPS-6 in paternal mitochondria is required to mediate PME. Because expression of the nuclease-deficient CPS-6(H148A) mutant in *cps-6(tm3222)* males failed to rescue the PME defect (Fig. 2F, matings 3 and 4), the nuclease activity of CPS-6 is essential for PME.

Using electron tomography, we examined how loss of *cps-6* affects PME. In *cps-6(tm3222)* zygotes, aggregates were still visible in paternal mitochondria but were smaller and fewer than in N2 zygotes, and no ghost PM were detected (Fig. 1, B, E, and G), indicating reduced and slower internal breakdown of paternal mitochondria. The autophagosome membranes started to assemble around paternal mitochondria in two- or four-cell *cps-6(tm3222)* embryos and completed enclosure by the 16-cell stage (Fig. 1, H and I), proceeding significantly slower than in N2 embryos, in which autophagosome assembly started earlier at the one-cell stage and was complete by the four-cell stage (Fig. 1, C to E). Even after autophagosome enclosure, internal breakdown of paternal mitochondria was clearly delayed (Fig. 1, I and J), because a significant portion of cristae remained superficially intact and fewer than 40% of paternal mitochondria transited into ghost PM in 16-cell

cps-6(tm3222) embryos (Fig. 1E). Some large agg PM even lingered on in 64-cell embryos (Fig. 1J), compared with 100% of paternal mitochondria either eliminated or becoming ghost PM by the four-cell N2 embryos (Fig. 1, D and E). Therefore, CPS-6 is important in mediating internal breakdown of paternal mitochondria and their enclosure by autophagosomes after fertilization.

Compromised mitochondria often show loss of membrane potential, which can be detected by tetramethylrhodamine ethyl ester (TMRE), a potential-sensitive mitochondrial dye. When N2 males prestained with TMRE and a nucleic acid dye (SYTO11)—which labeled sperm mitochondria and their mtDNA, respectively (fig. S4, A and B)—were mated with N2 hermaphrodites, paternal mitochondria were still labeled by SYTO11 in N2 zygotes, but their TMRE staining was completely lost (Fig. 3A). In comparison, staining of paternal mitochondria by potential-insensitive MTR persisted (fig. S4B). When we mated SYTO11-stained N2 males with N2 hermaphrodites in the presence of TMRE, only maternal mitochondria were stained by TMRE, and the SYTO11-positive paternal mitochondria were TMRE-negative (Fig. 3B). Therefore, paternal

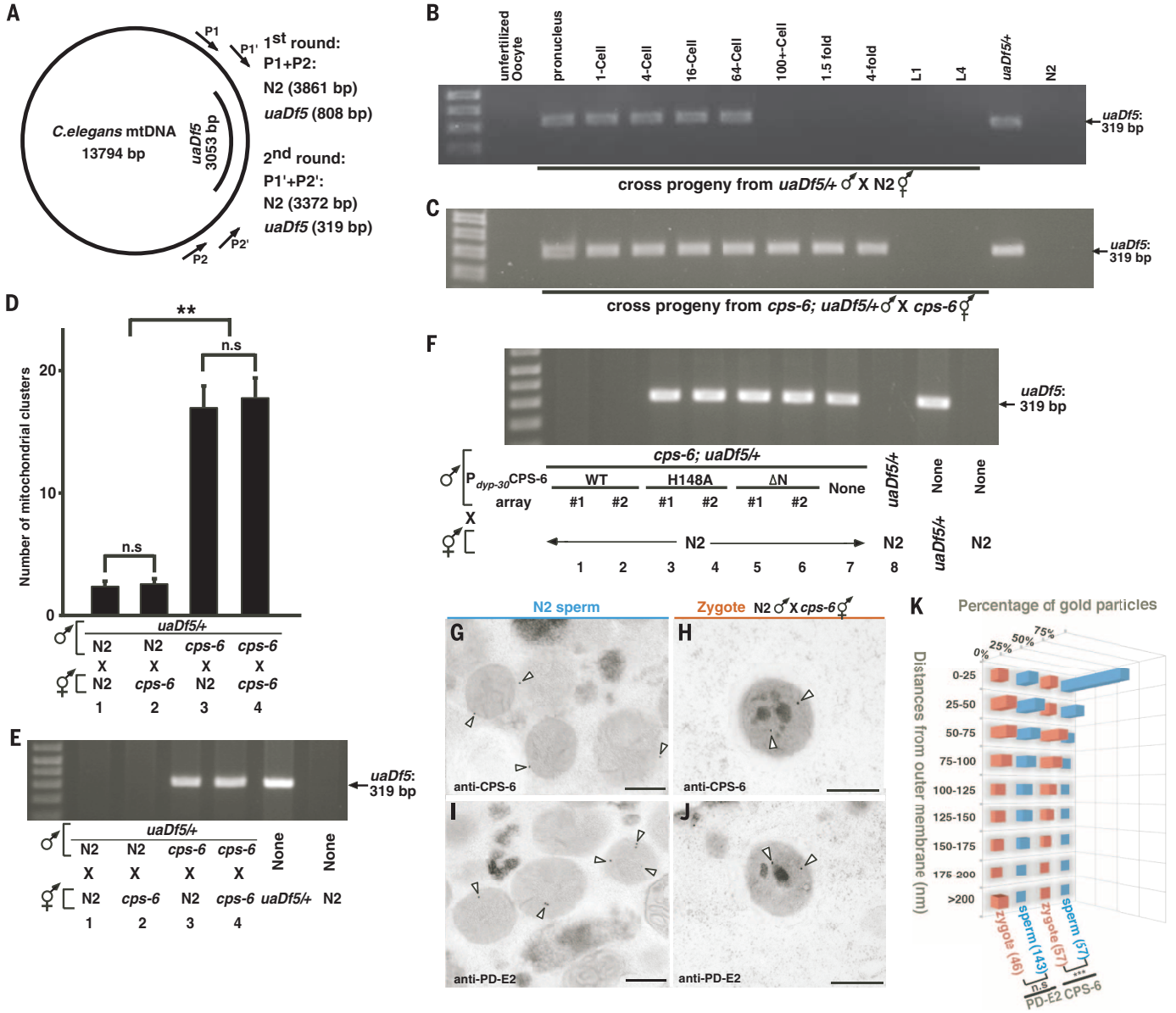

Fig. 2. CPS-6 relocates from the intermembrane space of paternal mitochondria to the matrix after fertilization to promote PME. (**A**) Diagram of *C. elegans* mtDNA, the *uaDf5* deletion, primers used in the nested PCR assays, and sizes of PCR products in N2 and *uaDf5/+* animals. (**B** and **C**) Hermaphrodites and MTR-stained males were mated as indicated. Males also carried *smIs42*, an integrated $P_{sur\text{-}5}$*sur-5::gfp* transgene used to track cross progeny (see fig. S2A). A single unfertilized oocyte and a single cross-fertilized embryo or larva (MTR- or GFP-positive) at the indicated stage was analyzed by PCR. *uaDf5/+* and N2 hermaphrodites were controls. (**D**) Quantification of MTR-stained paternal mitochondrial clusters in 64-cell embryos from the indicated crosses with MTR-stained males. Data are means ± SEM; n = 20 per cross. $^{**}P <$ 0.0001 (unpaired Student t test); n.s., not significant. (**E** and **F**) Five cross-fertilized embryos (E) or transgenic embryos (F) at approximately 100-cell stage from the indicated crosses were analyzed by PCR. (**G** to **J**) Representative immuno-EM images of mitochondria in N2 spermatozoa and paternal mitochondria in zygotes from the indicated cross. CPS-6–specific and PD-E2–specific immunogold particles are marked with arrowheads. Scale bars, 300 nm. (**K**) Histogram of the distances of 15-nm immunogold particles from the mitochondrial membrane, illustrating CPS-6's movement after fertilization. Numbers of immunogold particles scored are shown in parentheses. $^{***}P < 0.0001$ (Mann-Whitney U test). *cps-6(tm3222)* was used in all figures.

mitochondria are depolarized shortly after fertilization, preceding degradation of their mtDNA.

We used immuno-EM to determine the localization of CPS-6 in paternal mitochondria. CPS-6 immunogold particles were predominantly associated with the mitochondrial membrane in N2 spermatozoa (Fig. 2, G and K, and fig. S2G), in agreement with CPS-6's localization in mitochondrial intermembrane space. In zygotes from *cps-6(tm3222)* hermaphrodites mated with N2 males, CPS-6 immunogold particles were often located inside paternal mitochondria, away from the mitochondrial membrane (Fig. 2, H and K, and fig. S5). Because some paternal mitochondria had not been associated with autophagosomes (Fig. 2H), CPS-6 appeared to enter the matrix before the assembly of autophagosomes. The relocation of CPS-6 into the matrix after fertilization is clearly discerned when compared with the localization patterns of a mitochondrial matrix protein, the E2 subunit of pyruvate dehydrogenase (PD-E2, Fig. 2, I to K). Collectively, these different microscopy analyses provide strong evidence that paternal mitochondria are depolarized and damaged internally soon after fertilization, leading to the release of CPS-6 into the matrix to catalyze mtDNA degradation.

The autophagy and proteasome pathways promote PME in *C. elegans* (*5*–*7*). Both LGG-1, the worm LC3/Atg8 homolog necessary for autophagosome formation (*11*), and RAD-23, a ubiquitin receptor important for proteasomal degradation (*5*, *12*), act maternally to promote PME (fig. S6, A and B, and supplementary text). Analyses of the double and the triple mutants among *cps-6*, *lgg-1*, and *rad-23* indicate that *cps-6*, *lgg-1*, and *rad-23* use distinct mechanisms (mitochondrial self-destruction, autophagy, and proteasomes, respectively) to coordinate swift and efficient PME (fig. S6, C to F).

Because loss of *cps-6* slows down autophagosome formation and degradation of paternal mitochondria (Fig. 1), we further interrogated this issue by immunostaining; we found that in N2 zygotes, bright LGG-1 staining was seen clustering around MTR-stained paternal mitochondria near the site of sperm entry (fig. S4C), with 81% of paternal mitochondrial clusters colocalizing with LGG-1 autophagosomes (fig. S4E). By contrast, in *cps-6(tm3222)* zygotes, such colocalization dropped to 43% (fig. S4, D and E), indicating that loss of *cps-6* reduces autophagosome formation on paternal mitochondria. Analysis using superresolution structured illumination microscopy (SIM) revealed similar results. In N2 zygotes, the majority (77%) of paternal mitochondria were enclosed by LGG-1 autophagosomes, some (12%) were partially enclosed, and only 11% did not associate with (isolated) autophagosomes (Fig. 3, C and D, and fig. S4, F and H). By contrast, in *cps-6(tm3222)* zygotes, 51% of paternal mitochondria were isolated and only 29 and 20% of paternal mitochondria were enclosed and partially enclosed by autophagosomes, respectively (Fig. 3, E and F, and fig. S4, G and H). These findings indicate that the CPS-6 self-destruction process is important for efficient recruitment of autophagosomes to paternal mitochondria.

It has been suggested that the high rate of energy consumption during fertilization of an oocyte by many competing spermatozoa leads to increased oxidative damage and mutations in sperm mtDNA (*13*, *14*). Failure to remove paternal mitochondria with mutated mtDNA can cause incompatibility with maternal mitochondria and the nuclear genome and can adversely affect the fitness of animals (*15*–*17*). Comparison of N2 embryos with *uaDf5*/+ embryos, with four genes deleted in *uaDf5* mtDNA (*18*), revealed a factor of 23 increase in embryonic lethality from 0.4 to 9.4% (Fig. 4A, assays 1 and 3), indicating that the heteroplasmic presence of mtDNA mutations compromises embryo development. Delayed removal of *uaDf5* paternal mitochondria in embryos by loss of *cps-6* resulted in a lethality rate of 5.9%, higher by a factor of 5 to 7 than that of cross-fertilized *cps-6(tm3222)* embryos (0.7%) or that of embryos with no persistent paternal mitochondria (0.8 to 0.9%) (Fig. 4A, assays 4 to 7, and supplementary text). Moreover, delayed clearance of *uaDf5* paternal mitochondria slowed cell divisions, an energy-driven process, during *C. elegans* embryogenesis, because the average durations of cell divisions in two different cell lineages (MS and P) were significantly prolonged in *uaDf5*/+ embryos and by delayed removal of *uaDf5* paternal mitochondria (Fig. 4, B and C, fig. S7, and supplementary

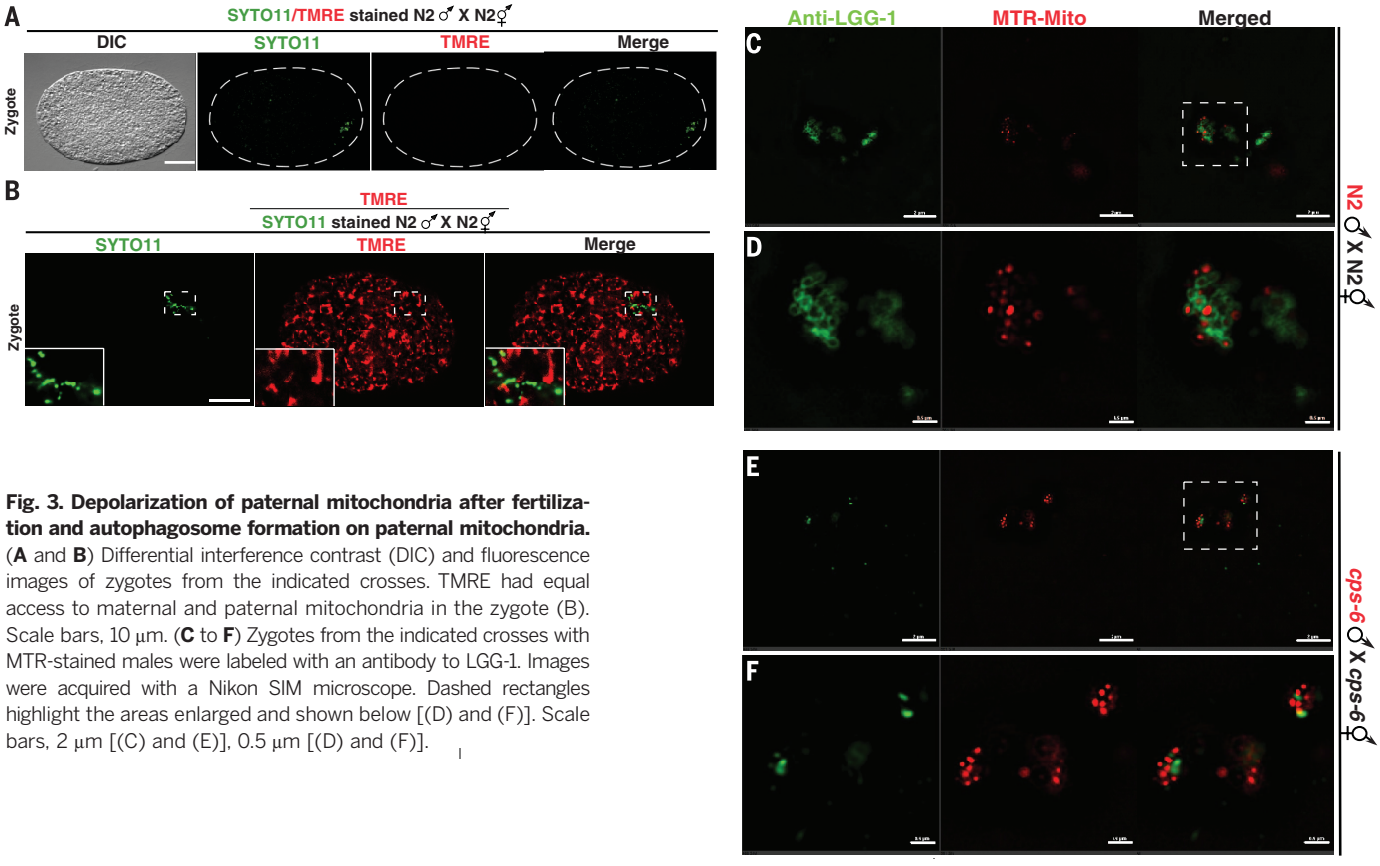

Fig. 3. Depolarization of paternal mitochondria after fertilization and autophagosome formation on paternal mitochondria. (**A** and **B**) Differential interference contrast (DIC) and fluorescence images of zygotes from the indicated crosses. TMRE had equal access to maternal and paternal mitochondria in the zygote (B). Scale bars, 10 μm. (**C** to **F**) Zygotes from the indicated crosses with MTR-stained males were labeled with an antibody to LGG-1. Images were acquired with a Nikon SIM microscope. Dashed rectangles highlight the areas enlarged and shown below [(D) and (F)]. Scale bars, 2 μm [(C) and (E)], 0.5 μm [(D) and (F)].

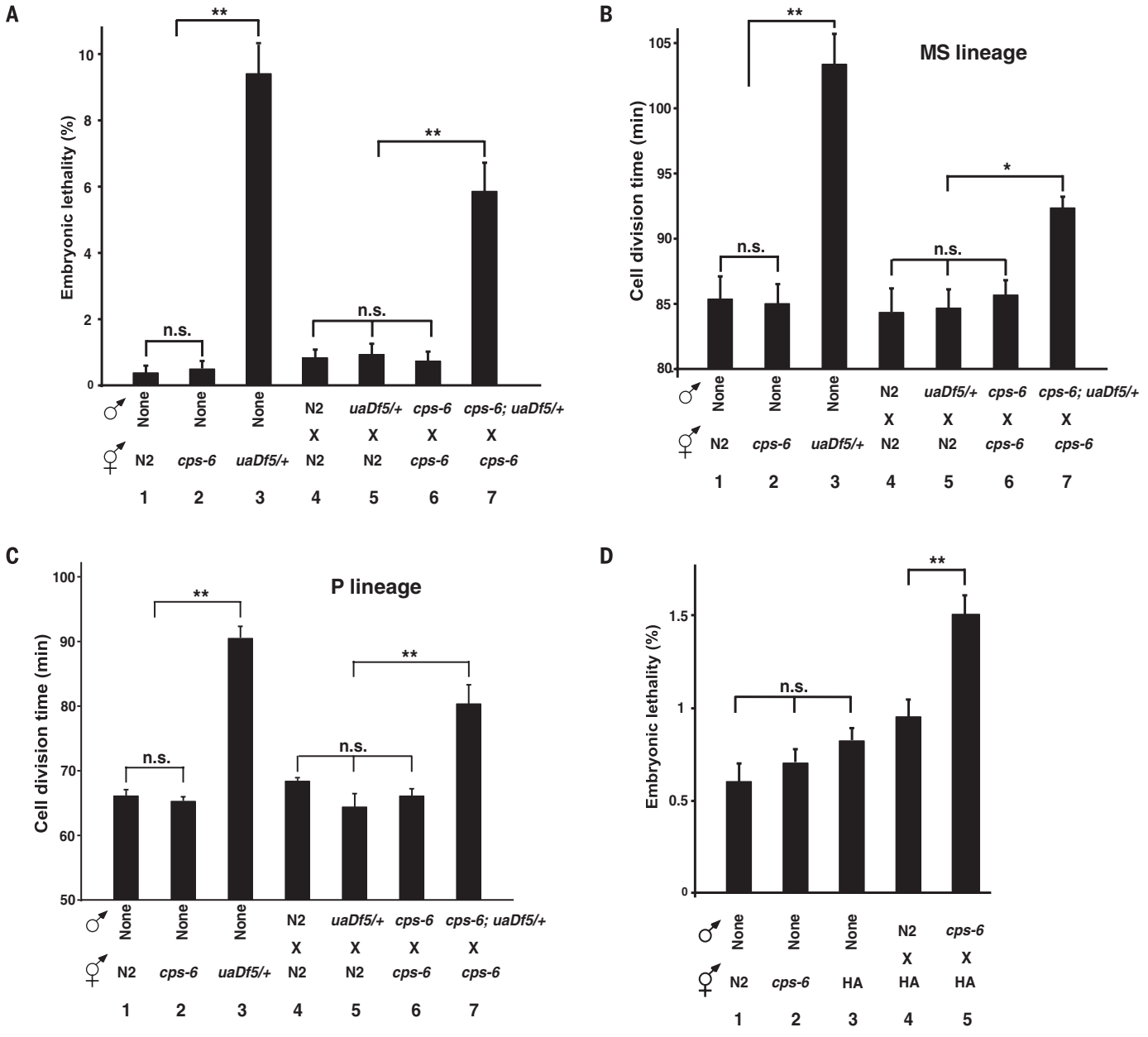

Fig. 4. Delayed removal of paternal mitochondria increases embryonic lethality and cell division durations. (**A** to **D**) The embryonic lethality rate [(A) and (D)] and durations of cell divisions in the MS lineage (B) and P lineage (C) were scored in self-fertilized embryos (1 to 3) or cross-fertilized embryos from crosses (4 to 7) of the indicated genotypes. All males carried *smIs42* and were stained with MTR to assist identification of zygotes [(B) and (C)]. Data are means ± SEM; $n > 1000$ embryos per cross at 25°C [(A) and (D)] and $n = 3$ embryos per cross at 20°C [(B) and (C)]. *$P < 0.05$, **$P < 0.001$ (unpaired Student t test).

text). These results provide evidence that delayed clearance of mutated paternal mitochondria leads to decreased fitness at the cellular and organismal levels and presents an evolutionary disadvantage.

Next, we examined the consequence of delayed removal of wild-type paternal mitochondria by mating two different *C. elegans* wild-type strains, the Bristol strain (N2) and the Hawaii strain (HA). Delayed removal of wild-type Bristol paternal mitochondria in HA embryos due to loss of paternal *cps-6* also resulted in a significantly higher percentage of embryonic lethality than that seen in HA embryos without persistent paternal mitochondria (Fig. 4D, assays 4 and 5, and fig. S6G, matings 2 and 4; see also supplementary text). Therefore, delayed clearance of wild-type paternal mitochondria slightly different from maternal mitochondria also compromises animal development, which suggests that transmission of paternal mitochondria among different wild-type variants is evolutionarily disadvantageous.

Our results show that soon after fertilization, paternal mitochondria are depolarized and lose their inner membrane integrity, which apparently marks them for degradation by autophagy (*19*, *20*). The inner membrane breakdown probably triggers the entry of the intermembrane CPS-6 into the matrix of paternal mitochondria to degrade mtDNA, which encodes 12 mitochondrial proteins, two rRNAs, and 22 tRNAs that are essential for normal functions and maintenance of mitochondria (*1*, *13*, *18*). Degradation of mtDNA is detrimental, which accelerates breakdown of paternal mitochondria and could promote externalization of signals recognized by the autophagy or proteasome machinery (*19*, *20*), leading to PME (fig. S8). Consistent with this model, loss of paternal *cps-6* delays internal breakdown of paternal mitochondria and their enclosure and degradation by the autophagy

machinery. Interestingly, delayed removal of either mutant or slightly different wild-type paternal mitochondria results in increased embryonic lethality in heteroplasmic animals, likely due to incompatibility in cellular signaling between the mitochondrial and nuclear genomes (*15*, *17*). This provides evidence that persistence of paternal mitochondria compromises animal development and may be the impetus for maternal inheritance of mitochondria. DeLuca and O'Farrell showed that endonuclease G mediated the degradation of sperm mitochondrial DNA during *Drosophila* spermatogenesis before fertilization and hypothesized that this degradation helped prevent paternal mtDNA transmission (*21*). In contrast, we find in *C. elegans* that CPS-6 acts after fertilization to mediate degradation of both paternal mitochondria and mtDNA to facilitate their autophagic degradation. These findings imply a conserved role of endonuclease G in paternal mtDNA elimination and expand the roles of this nuclease beyond apoptosis and mitochondrial maintenance (*8*, *9*, *22*).

REFERENCES AND NOTES

1. S. E. Calvo, V. K. Mootha, *Annu. Rev. Genomics Hum. Genet.* **11**, 25–44 (2010).
2. X. Wang, *Genes Dev.* **15**, 2922–2933 (2001).
3. M. Sato, K. Sato, *Biochim. Biophys. Acta* **1833**, 1979–1984 (2013).
4. B. Levine, Z. Elazar, *Science* **334**, 1069–1070 (2011).
5. Q. Zhou, H. Li, D. Xue, *Cell Res.* **21**, 1662–1669 (2011).
6. S. Al Rawi *et al.*, *Science* **334**, 1144–1147 (2011).
7. M. Sato, K. Sato, *Science* **334**, 1141–1144 (2011).
8. J. Parrish *et al.*, *Nature* **412**, 90–94 (2001).
9. L. Y. Li, X. Luo, X. Wang, *Nature* **412**, 95–99 (2001).
10. J. L. Lin *et al.*, *J. Biol. Chem.* **287**, 7110–7120 (2012).
11. K. Jia, B. Levine, *Adv. Exp. Med. Biol.* **694**, 47–60 (2010).
12. K. Madura, *Trends Biochem. Sci.* **29**, 637–640 (2004).
13. D. C. Wallace, *Environ. Mol. Mutagen.* **51**, 440–450 (2010).
14. J. M. Cummins, *Hum. Reprod.* **15** (suppl. 2), 92–101 (2000).
15. M. S. Sharpley *et al.*, *Cell* **151**, 333–343 (2012).
16. M. Schwartz, J. Vissing, *N. Engl. J. Med.* **347**, 576–580 (2002).
17. N. Lane, *BioEssays* **33**, 860–869 (2011).
18. W. Y. Tsang, B. D. Lemire, *Biochem. Cell Biol.* **80**, 645–654 (2002).
19. G. Ashrafi, T. L. Schwarz, *Cell Death Differ.* **20**, 31–42 (2013).
20. K. Wang, D. J. Klionsky, *Autophagy* **7**, 297–300 (2011).
21. S. Z. DeLuca, P. H. O'Farrell, *Dev. Cell* **22**, 660–668 (2012).
22. C. McDermott-Roe *et al.*, *Nature* **478**, 114–118 (2011).

ACKNOWLEDGMENTS

We thank T. Blumenthal, R. Poyton, and K. Krauter for comments and H. Zhang for strains and antibodies. Supported by March of Dimes grant 1-FY14-300 and NIH grants GM59083, GM79097, and GM118188 (D.X.) and Research Grants Council of Hong Kong grant AoE/M-05/12 (B.-H.K.).

SUPPLEMENTARY MATERIALS

www.sciencemag.org/content/353/6297/394/suppl/DC1
Materials and Methods
Supplementary Text
Figs. S1 to S8
Table S1
Movie S1
References (*23*–*37*)

14 February 2016; accepted 15 June 2016
Published online 23 June 2016
10.1126/science.aaf4777

CANCER IMMUNOTHERAPY

Cdk5 disruption attenuates tumor PD-L1 expression and promotes antitumor immunity

R. Dixon Dorand,[1,2] Joseph Nthale,[2,3] Jay T. Myers,[2,3] Deborah S. Barkauskas,[2,3] Stefanie Avril,[1,4] Steven M. Chirieleison,[1] Tej K. Pareek,[2,3] Derek W. Abbott,[1,4] Duncan S. Stearns,[2,3,4] John J. Letterio,[2,3,4] Alex Y. Huang,[1,2,3,4]*† Agne Petrosiute[2,3,4]*†

Cancers often evade immune surveillance by adopting peripheral tissue–tolerance mechanisms, such as the expression of programmed cell death ligand 1 (PD-L1), the inhibition of which results in potent antitumor immunity. Here, we show that cyclin-dependent kinase 5 (Cdk5), a serine-threonine kinase that is highly active in postmitotic neurons and in many cancers, allows medulloblastoma (MB) to evade immune elimination. Interferon-γ (IFN-γ)–induced PD-L1 up-regulation on MB requires Cdk5, and disruption of Cdk5 expression in a mouse model of MB results in potent $CD4^+$ T cell–mediated tumor rejection. Loss of Cdk5 results in persistent expression of the PD-L1 transcriptional repressors, the interferon regulatory factors IRF2 and IRF2BP2, which likely leads to reduced PD-L1 expression on tumors. Our finding highlights a central role for Cdk5 in immune checkpoint regulation by tumor cells.

Cyclin-dependent kinase 5 (Cdk5) is a nonstereotypical Cdk whose activity depends on coactivators, p35 and/or p39. A proline-directed serine-threonine kinase (*1*), Cdk5 is essential in central nervous system (CNS) development (*2*, *3*). Cdk5 also contributes to angiogenesis, apoptosis, myogenesis, vesicular transport, and senescence in nonneuronal cells, including tumors (*4*–*6*), which makes Cdk5 a potential therapeutic target in cancers (*7*–*9*). We explored whether Cdk5 plays a role in medulloblastoma (MB), a common malignant pediatric CNS tumor.

MB cell lines and clinical specimens expressed Cdk5, p35, and p39 (Fig. 1A and fig. S1A). Cdk5-specific kinase activity could be abolished in vitro by roscovitine, a nonselective inhibitor against Cdks 1, 2, 5, 7, and 9 (fig. S1B) (*10*). To interrogate Cdk5-specific functions, we disrupted Cdk5 in wild-type murine MB cells (MM1 WT) by short hairpin–mediated RNA interference (MM1 shCdk5) and clustered regularly interspaced short palindromic repeats (CRISPR)–Cas9–targeted mutation (MM1 crCdk5), with nontargeting constructs as controls (MM1 shNS and MM1 crNeg). A reduction in Cdk5 was confirmed at the transcript (fig. S1C) and protein levels (fig. S1D). In vitro, there were no significant differences in cell proliferation among all constructs (fig. S1, E and F) (*1*).

[1]Department of Pathology, Case Western Reserve University School of Medicine, Cleveland, OH 44106, USA. [2]Division of Pediatric Hematology-Oncology, Department of Pediatrics, Case Western Reserve University School of Medicine, Cleveland, OH 44106, USA. [3]Angie Fowler Adolescent and Young Adult Cancer Institute and University Hospitals Rainbow Babies and Children's Hospital, Cleveland, OH 44106, USA. [4]Case Comprehensive Cancer Center, Case Western Reserve University School of Medicine, Cleveland, OH 44106, USA.
*These authors contributed equally to this work. **†Corresponding author. Email: ayh3@case.edu (A.Y.H.); axp125@case.edu (A.P.)**

To assess MB growth in vivo, 5×10^4 Cdk5-deficient or control cells were inoculated subcutaneously (s.c.) into the flanks of immunodeficient mice. All mice developed comparable-sized tumors by day 14 (fig. S2, A to C). However, 78 to 50% of C57BL/6 mice injected s.c. with Cdk5-deficient MB cells showed tumor-free survival (TFS) at 19 and 42 days, whereas mice injected with WT and control tumors exhibited 0 and 7% TFS after 19 days, respectively (Fig. 1B and fig. S3A). Mice injected with Cdk5-deficient MB cells developed significantly smaller tumors (0.02 ± 0.04 g) than mice injected with WT (0.91 ± 0.39 g) or NS (0.51 ± 0.21 g) cells (fig. S3B). These data suggest a T cell–dependent rejection mechanism of Cdk5-deficient MM1 cells. This interpretation is supported by the observation that Cdk5 expression inversely correlated with T cell infiltration in human MB (Fig. 1C and fig. S2D).

To identify T cell populations mediating this potent rejection, we depleted $CD8^+$ T cells, $CD4^+$ T cells, or both subsets in mice inoculated with MM1 crCdk5 or crNeg cells (5×10^4 s.c.). By day 11, 100% of mice injected with MM1 crNeg and 80% of mice receiving MM1 crCdk5 developed measurable tumors (Fig. 1B), although MM1 crNeg tumors were 8 times the size of MM1 crCdk5 tumors (808.8 ± 382.1 versus 101.1 ± 92.9 mm^3) (Fig. 1D). Depletion with CD4-specific (αCD4) antibody alone or with both αCD4 and αCD8 antibodies resulted in 100% MM1 crCdk5 tumor incidence accompanied by rapid tumor growth, whereas CD8 depletion alone yielded 30% TFS, similar to isotype control (Fig. 1D). Among mice receiving isotype antibody, three of eight crCdk5 tumor outgrowths regressed starting on day 17, whereas three of nine crCdk5 tumor outgrowths among mice depleted of $CD8^+$ T cells regressed starting on day 25; these outgrowths contributed

Editor's Summary

Eliminating paternal mitochondria

During fertilization, the oocyte and sperm each bring their mitochondria to the union. Shortly afterward, the paternal mitochondria are degraded, and only the maternal mitochondria are conveyed to the progeny. Zhou *et al.* observed that the integrity of the inner membrane of paternal mitochondria is compromised, which apparently marks them for degradation (see the Perspective by van der Bliek). Autophagy commences by mitochondrial endonuclease G relocating from the intermembrane space into the matrix and subsequently degrading the paternal mitochondrial DNA. Any delay in this process increases embryonic lethality.

Science, this issue p. 394; see also p. 351

Supplementary Materials for

Mitochondrial endonuclease G mediates breakdown of paternal mitochondria following fertilization

Qinghua Zhou, Haimin Li, Hanzeng Li, Akihisa Nakagawa, Jason L.J. Lin, Eui-Seung Lee, Brian L. Harry, Riley Robert Skeen-Gaar, Yuji Suehiro, Donna William, Shohei Mitani, Hanna S. Yuan, Byung-Ho Kang†, and Ding Xue†

Correspondence to: ding.xue@colorado.edu or bkang@cuhk.edu.hk

This PDF file includes:

Other Supplementary Materials for this manuscript includes the following:

Materials and Methods

Identification of candidate *C. elegans* genes that encode mitochondrial proteins

To identify candidate *C. elegans* genes that encode proteins residing in mitochondria, we took advantage of the comprehensive mitochondrial compendium of 1098 genes identified from 14 mouse tissues *(23)*. We blasted the *C. elegans* genome to identify orthologs of these 1098 mitochondrial proteins. Excluding those genes that are redundant or genes whose RNAi treatment results in embryonic lethality, we identified 217 candidate genes that encode mitochondrial proteins in *C. elegans* for the RNAi screen (table S1). The DNA and protein sequences of all genes listed in this paper can be obtained from the wormbase (http://www.wormbase.org).

RNAi screen

To identify mitochondrial proteins involved in PME, we performed RNAi screen on 217 candidate genes predicted to encode mitochondrial proteins in *C. elegans,* using a sensitive nested PCR assay to detect the presence of paternal *uaDf5* mtDNA (Fig. 2A). A bacterial feeding protocol of RNAi was used to treat plates containing *uaDf5*/+ males and *fem-3(e1996) dpy-20(e1282)* animals, which are fertile females lacking sperm and thus cannot self-fertilize *(24)*. Cross progeny at late embryonic stages or early larval stages were subject to the PCR screen to search for the presence of *uaDf5* paternal mtDNA. Each RNAi experiment was carried out in duplicate at room temperature. The RNAi experiments that produced single positive or double positive results (presence of *uaDf5* mtDNA) were retested in duplicate, and sometimes, in multiple (4 to 8) replication experiments. RNAi treatment of one gene, C41D11.8 (*cps-6*), was found to be positive in multiple retests and was analyzed further.

Strains

C. elegans strains were maintained at 20°C using standard methods *(25)*. The alleles used for this study: LGI, *cps-6 (tm3222);* LGII, *lgg-1(bp500), rad-23(tm2595);* LGIV, *fem-3(e1996)*, *dpy-20(e1282), him-8(e1489);* mtDNA, *uaDf5 (18)*. *smIs42* is an integrated transgene generated by gamma irradiation of animals carrying an extrachromosomal array containing $P_{sur\text{-}5}$*sur-5::gfp*. It was backcrossed four times with N2 animals before being used in this study.

Transgenic animals

Complex transgenic arrays were generated as previously described to promote germline expression of the transgenes *(26)*. Briefly, *cps-6(tm3222); uaDf5*/+ worms were injected with 10 ng/µL of $P_{sur\text{-}5}$*sur-5::gfp* (injection marker), 2.5 ng/µL of $P_{dpy\text{-}30}$CPS-6 (wild-type, **Δ**N, or H148A), and 500 ng/µL Sca I-digested N2 genomic DNA.

MitoTracker Red (MTR), SYTO 11, and TMRE staining

1 mM MTR in dimethyl sulfoxide (DMSO) was diluted in M9 buffer (42.3 mM Na_2HPO_4, 22 mM KH_2PO_4, 8.6 mM NaCl, 18.7 mM NH4Cl) to a final concentration of 50 μM before mixing with *E. coli* OP50 to feed *C. elegans* animals. L4 larval stage males were fed with the MTR/bacteria mixture for 12 hours and then cleaned up through three rounds of "bacterial shower", in which they were transferred to a fresh plate with unstained OP50 for 15 minutes each to remove MTR from their exterior. Subsequently, MTR-stained males were mated with unstained young adult hermaphrodites for 8 hours before the mated hermaphrodites were dissected to obtain cross-fertilized MTR-stained oocytes. For SYTO11 and TMRE staining, the same protocol was used. The final concentrations of SYTO11 and TMRE used were 10 μM and 50 μM, respectively.

Fluorescent and time-lapse microscopy

Fluorescent and time-lapse microscopy was performed as described previously *(27)*. Briefly, mated hermaphrodites as described above were dissected and embryos were released onto an agarose pad. A coverslip was then applied on the embryos and egg salt buffer [118 mM NaCl, 48 mM KCl, 2 mM $CaCl_2$, 2 mM $MgCl_2$, and 5 mM HEPES (pH 7.5)] was pipetted into the empty space between the coverslip and the slide. The sample was sealed with a hot mixture of petrol gel and bees wax. Images were captured from the top to the bottom of the embryo using a Zeiss Axioplan 2 microscope equipped with a Cohu CCD camera and SlideBook 5 software (Intelligent Imaging Innovations, Inc.). Z-stacks were then deconvolved and projected into one plane to depict all MTR-stained mitochondria from an embryo in a single image. The duration from the MS cell to the MS.aaaa cell or from the P1 cell to the P4 cell was determined as described previously *(27)*.

Quantification of MTR-stained paternal mitochondrial clusters in fertilized oocytes

The number of MTR fluorescent dots was scored from deconvolved images of fertilized oocytes or embryos derived from mating of MTR-stained males with unstained hermaphrodites. For each genotype, 20 cross-fertilized embryos were scored.

PCR analysis

Single or multiple cross-fertilized embryos or larvae at various developmental stages were dissected from mated hermaphrodites or collected from the mating plates and analyzed by PCR. The primer pairs used to detect the *uaDf5* deletion are: P1, 5' GATTAGCACAAGCTTTATTGGATGG 3' and P2, 5' AAGATCTTAACATTCCGGCTGAGGC 3'; P1', 5' TGGTATAATTGGGGCCATCCGTGC 3' and P2', 5' AGGGTCTTCTACAGTGCATTGACC 3'.

Electron microscopy and electron tomography

Mated *C. elegans* hermaprodites were processed by high-pressure freezing, freeze-substitution, and embedding in epoxy resin as described previously *(28)*. To prepare samples for immunogold labeling, worms were freeze-substituted in anhydrous acetone containing 0.1% UA and 0.25% glutaraldehyde and embedded in LRwhite resin. Sectioning, staining, immunogold labeling, and EM imaging were performed according to a previous protocol *(29)*, with a Spirit electron microscope (FEI, Hillsboro, OR, USA). 15 nm gold particles are conjugated to a secondary antibody against rabbit immunoglobulin G. Electron tomography analysis was carried out as described previously *(30)*. In brief, 250 nm thick sections were collected and the sections were coated with fiducial particles. Tilting series images from 2 orthogonal axes were collected at 15400X from +60º to -60º with 1.5 increments using a TF20 electron microscope (FEI, Hillsboroa, OR, USA). Tomograms were calculated using the Etomo module of the IMOD software package (Boulder Laboratory of 3D Electron Microscopy of the Cell, University of Colorado at Boulder). 3D models were generated with the 3dmod program in the same package.

RNAi experiments

All RNAi experiments were carried out at room temperature using a bacterial feeding protocol *(26)* and RNAi bacterial clones from a *C. elegans* RNAi library (constructed by the Ahringer laboratory). For *cps-6*(RNAi) experiments, animals were treated with RNAi for two generations before their progeny were examined for defects in apoptosis and PME.

Embryonic lethality assays

The assays were carried out at 25°C. For self-fertilized strains, late L4 larvae were aged for 12 hours and then transferred to fresh plates to lay eggs for 6 hours before they were

removed. The total number of embryos in the plates was then scored. After 24 hours, embryos that did not hatch were scored as dead embryos. Embryonic lethality rate was calculated as the number of dead embryos divided by the total number of embryos. For cross-fertilized strains, late L4 hermaphrodites were mated with young adult *smIs42* males with the indicated genotype for 12 hours and then transferred to fresh plates to lay eggs for 6 hours before they were removed. Embryonic lethality rate was calculated similarly as the number of dead GFP-positive embryos divided by the total number of GFP-positive embryos.

Quantification of paternal mitochondria in dividing embryos

Quantification of paternal mitochondria in dividing embryos was conducted as described previously with minor modifications *(5)*. Briefly, the numbers of MTR-stained mitochondrial clusters were scored from deconvolved images of the fertilized egg at different embryonic stages. The number of paternal mitochondrial clusters for each fertilized egg at the 1-cell stage was set artificially at 100. Relative numbers of paternal mitochondrial clusters in other embryonic stages of the same fertilized egg were normalized using the 1-cell stage number. To avoid photobleaching and to achieve maximal quantification accuracy, we followed cell divisions in the fertilized egg by DIC and acquired fluorescent images manually at specific embryonic stages.

Immunofluorescence imaging by widefield fluorescent microscopy and Structured Illumination Microscopy (SIM)

Immunostaining of *C. elegans* embryos was performed as described previously *(31)*, using an anti-LGG-1 mouse monoclonal antibody (1:100; provided by Hong Zhang, Institute of Biophysics, Beijing, China). Secondary antibodies used are FITC-conjugated goat anti-mouse antibody (1:100; Jackson ImmunoResearch laboratories, Inc.). Stained embryos were mounted

onto the slides with Vectashield Antifade Mounting Medium with DAPI. Widefield fluorescent microscopy images were captured from the top to the bottom of the embryos using a Zeiss Axioplan 2 microscope equipped with a Cohu CCD camera and a SlideBook 5 software (Intelligent Imaging Innovations, Inc.). Z-stacks were then deconvolved and projected into one plane to depict all MTR-stained mitochondria from an embryo in a single image. SIM imaging is achieved by enlarging the Fouriet Domain of sample images about two fold with Nikon Structured Illumination Microscopy (N-SIM). Stained embryos were imaged with 488 nm and 561 nm channels (100X, oil lens).

Quantification of co-localization or encapsulation of paternal mitochondria by autophagosomes in fertilized oocytes

Using widefield fluorescent microscopy images, the co-localization ratio of paternal mitochondrial clusters with autophagosomes in fertilized oocytes is determined as the number of MTR-stained mitochondrial clusters that are associated with LGG-1 immunofluorescence signals divided by the total number of MTR-stained mitochondrial clusters. Using SIM images, the percentages of three classes of paternal mitochondria are determined: those fully encapsulated by autophagosomes (enclosed), those partially encapsulated by autophagosomes (partially enclosed), and those that are not associated with any autophagosome (isolated).

Constructs. The *cps-6* expression constructs used in the study were made in previous studies *(8, 10)*.

Supplementary Text

CPS-6 acts in paternal mitochondria to promote PME

cps-6 was first identified as a nuclease-encoding gene that acts downstream of the CED-3 caspase to mediate chromosome fragmentation during apoptosis *(8)*. Inactivation of *cps-6* causes a delay in embryonic cell death and accumulation of 3′ hydroxyl DNA breaks that can be labeled by TUNEL [terminal deoxynucleotidyl transferase (TdT)–mediated dUTP nick end labeling]*(8)*. CPS-6 resides in mitochondria in normal cells, but is released from mitochondria during apoptosis and translocates to the nucleus to meidate chromosome fragmentation *(8, 9)*. We first examined if the activity of CPS-6 is required paternally, maternally, or both to promote PME. *uaDf5*/+ males or *cps-6(tm3222); uaDf5*/+ males stained by MTR were mated with either N2 hermaphrodites or *cps-6(tm3222)* hermaphrodites. 64-cell stage cross-fertilized embryos were scored for the number of MTR-stained paternal mitochondrial clusters by microscopic analysis (Fig. 2D). In parallel, we examined the presence of *uaDf5* paternal mtDNA by PCR analysis of cross-fertilized embryos at approximately 100-cell stage (Fig. 2E). In both assays, a significant portion of paternal mitochondria and mtDNA persisted past the 64-cell embryonic stage when *cps-6* was eliminated from the paternal lineage (Fig. 2, D and E, mating 3, 4). On the other hand, absence of maternal *cps-6* in the oocyte still resulted in rapid and close to complete PME by the 64-cell stage as in N2 fertilized oocytes (Fig. 2, D and E, mating 2). These results indicate that paternal CPS-6, but not maternal CPS-6, is specifically required to promote PME.

We then examined if CPS-6 is required within paternal mitochondria to mediate PME. CPS-6 contains a mitochondrial targeting sequence (amino acids 1-21) that is critical for its mitochondrial localization *(8)*. A CPS-6 mutant protein without this targeting sequence, CPS-6**Δ**N, localizes instead to the nucleus *(8)*. We generated *cps-6(tm3222); uaDf5*/+ transgenic animals expressing wild-type CPS-6 or CPS-6**Δ**N under the control of the promoter of the *dpy-*

30 gene ($P_{dpy\text{-}30}$CPS-6 and $P_{dpy\text{-}30}$CPS-6ΔN), which is ubiquitously expressed in *C. elegans (32)*. Transgenic *cps-6(tm3222); uaDf5*/+ males were mated with N2 hermaphrodites and cross-fertilized transgenic embryos at approximately the 100-cell stage were analyzed by PCR for the presence of *uaDf5* paternal mtDNA. Expression of wild-type CPS-6 in *cps-6(tm3222)* males rescued the defect in paternal mtDNA elimination (Fig. 2F, mating 1, 2, 7), whereas expression of CPS-6ΔN failed to do so (Fig. 2F, mating 5, 6). This result indicates that localization of CPS-6 in paternal mitochondria is required for CPS-6 to mediate PME. On the other hand, expression of either CPS-6 or CPS-6ΔN was sufficient to rescue the delay-of-cell-death defect in the *cps-6(tm3222)* mutant (fig. S2, D and E), in which some of the early embryonic cell deaths were delayed until the mid- or late embryonic stages (2-fold, 2.5-fold and 3-fold stages), resulting in the peak of embryonic cell deaths at the 2-fold embryonic stage *(8)*. This result indicates that the pro-apoptotic function of CPS-6 is distinct from its non-apoptotic function in PME. However, the nuclease activity of CPS-6 is required for both functions, as expression of CPS-6(H148A), which has no nuclease activity due to the replacement of the catalytic residue His148 by Ala (10), failed to rescue the defects in both cell death and PME (Fig. 2F, mating 3, 4 and fig. S2F). Therefore, both the nuclease activity and mitochondrial localization are required for CPS-6 to mediate PME.

The autophagy and proteasome pathways act maternally to promote PME

Previous reports have shown that the autophagy process and the proteasome pathway play important roles in degradation of paternal mitochondria in *C. elegans* embryos *(5-7)*. We examined if *lgg-1,* a critical autophagy gene *(11, 33)*, or *rad-23,* which encodes a ubiquitin receptor important for proteasomal degradation *(12)*, acts paternally or maternally to promote PME, using a loss-of-function *lgg-1(bp500)* mutation and a loss-of-function *rad-23(tm2595)*

deletion mutation. We quantified the number of MTR-stained paternal mitochondrial clusters in 64-cell stage cross-fertilized embryos derived from MTR-stained N2 or mutant males mated with unstained N2 or the corresponding mutant hermaphrodites. In both cases, when maternal *lgg-1* or *rad-23* was deficient, significantly more MTR-stained paternal mitochondria persisted regardless of the male genotype (fig. S6, A and B), with *rad-23(tm2595)* showing a weaker effect. These results indicate that unlike CPS-6 both LGG-1 and RAD-23 act maternally to promote PME.

cps-6 acts in parallel to maternal *lgg-1* and *rad-23* to promote PME

To examine the relationship between *cps-6* and *lgg-1,* we stained N2 males, *cps-6(tm3222)* or *lgg-1(bp500)* single mutant males, and *cps-6(tm3222); lgg-1(bp500)* double mutant males with MTR and mated them with respective unstained hermaphrodites. The resulting 64-cell stage cross-fertilized embryos were scored for the number of MTR-stained paternal mitochondrial clusters (fig. S6C). Cross-fertilized *cps-6(tm3222)* embryos and *lgg-1(bp500)* embryos had comparable numbers of MTR-stained paternal mitochondria, which were significantly higher than that from cross-fertilized N2 embryos (fig. S6C, mating 1-3). Importantly, loss of both *cps-6* and *lgg-1* resulted in a greater increase in MTR-stained paternal mitochondria compared to either mutant alone (fig. S6C, mating 4), indicating that *cps-6* and *lgg-1* act in different pathways to promote PME. This was confirmed by time-lapse microscopic analysis of cross-fertilized embryos at multiple stages of embryo development (fig. S6D). Similarly, loss of both *cps-6* and *rad-23* resulted in a significantly higher number of persistent paternal mitochondria than in either single mutant alone (fig. S6E), indicating that *cps-6* and *rad-23* also act in different pathways to mediate PME. Finally, an even higher number of persistent paternal mitochondria was observed in *cps-6(tm3222); lgg-1(bp500)* cross-fertilized embryos treated

with *rad-23(RNAi),* which is as efficient as *rad-23(tm2595)* in delaying PME (fig. S6, B and F), than in *cps-6(tm3222); lgg-1(bp500)* cross-fertilized embryos treated with control RNAi (fig. S6F). These results indicate that *cps-6, lgg-1,* and *rad-23* appear to function in three different pathways to coordinate elimination of paternal mitochondria. Because loss of *cps-6* compromises autophagosome formation on paternal mitochondria (Fig. 1, Fig. 3, C to F, and fig. S4, C to H), the *cps-6*-mediated mitochondrial self-destruction pathway also interacts with and regulates the execution of the autophagy pathway.

Delayed removal of paternal mitochondria increases embryonic lethality

We investigated the physiological consequence of delayed removal of paternal mitochondria to the proper development of animals. It has been suggested that the high rate of oxidative phosphorylation to generate energy necessary for successful fertilization of an oocyte among millions of competing spermatozoa leads to increased oxidative damage, and thus, a higher rate of mutations in paternal mtDNA *(14, 34, 35)*. Failure to remove paternal mitochondria carrying mutated mtDNA may result in incompatibility with maternal mitochondria and the nuclear genome and adversely affect the fitness of the animals *(14-16)*. To test this hypothesis, we first took advantage of the *uaDf5* deletion, which removes 4 of the 12 mitochondrial respiratory chain subunits encoded by mtDNA *(18)*, to determine if delayed removal of mutant paternal mitochondria affects normal embryo development. Comparison of N2 and *uaDf5*/+ embryos reveals a 23-fold increase in embryonic lethality from 0.4% to 9.4% (Fig. 4A, assays 1 and 3), suggesting that the heteroplasmic presence of the mutant mtDNA compromises embryonic development. When *uaDf5*/+ males were mated with N2 hermaphrodites, cross-fertilized embryos displayed a lethality rate of 0.9% (Fig. 4A, assay 5), which is comparable to that (0.8%) seen in cross-fertilized embryos between N2 males and hermaphrodites (Fig. 4A, assay

4). By contrast, embryos derived from mating between *cps-6(tm3222); uaD5f*/+ males and *cps-6(tm3222)* hermaphrodites contained persistent *uaD5f* paternal mitochondria (Fig. 2C) and experienced a lethality rate of 5.9%, an 8.4-fold increase over that (0.7%) of embryos from mating between *cps-6(tm3222)* males and *cps-6(tm3222)* hermaphrodites (Fig. 4A, assays 6 and 7). These results support the notion that inefficient clearance of mutant paternal mitochondria, even in a heteroplasmic mixture with wild-type maternal mitochondria, can significantly compromise embryo development and organismal fitness.

Given that mitochondria are the major energy-generating organelles and cell division is an energy-driven process, we examined if delayed removal of *uaDf5* paternal mitochondria affects the rate of cell division during embryogenesis using the invariant cell lineage in *C. elegans*. During normal embryogenesis, the MS.aaaa cell arises following 4 cell divisions of the mesodermal (MS) precursor cell and its anterior daughter cells (fig. S7, A to C)*(36)*. In N2 and *cps-6(tm3222)* embryos, this process occurs in about 85 minutes (Fig. 4B, assays 1 and 2). In *uaDf5*/+ embryos, this series of cell divisions was prolonged (103 minutes; Fig. 4B, assay 3), indicating that the heteroplasmic presence of mutant mitochondria interferes with proper cell division. While cross-fertilized embryos between N2 males and hermaphrodites or between *cps-6(tm3222)* males and hermaphrodites showed normal MS to MS.aaaa durations (84-86 minutes; Fig. 4B, assays 4 and 6), the average duration of MS to MS.aaaa (92 minutes) in cross-fertilized embryos between *cps-6(tm3222); uaDf5*/+ males and *cps-6(tm3222)* hermaphrodites was significantly longer than that in cross-fertilized embryos between *uaDf5*/+ males and N2 hermaphrodites (85 minutes; Fig. 4B, assays 5 and 7), in which *uaDf5* paternal mitochondria were removed efficiently (Fig. 2B). Similar results were obtained with another cell lineage, the P cell lineage, using the same assays (Fig. 4C; fig. S7, A and D). Therefore, both cell division

rates and viability of embryos are compromised by delayed removal of mutant paternal mitochondria. Since *uaDf5* is used to simulate accumulation of harmful mutations in mtDNA over multiple generations or a sporadic mutation that inactivates a crucial gene in mtDNA, these findings provide important proof-of-concept evidence that impaired clearance of mutated paternal mitochondria can lead to decreased fitness at the cellular and organismal levels.

We last examined the physiological consequence of delayed removal of wild-type paternal mitochondria. To interrogate this issue, we mated two different wild-type *C. elegans* strains, the Bristol strain (N2) and the Hawaii strain (HA), with each other. As in cross-fertilized N2 embryos from mating of N2 males and hermaphrodites (fig. S6A), the N2 or HA paternal mitochondria are rapidly cleared by the 64-cell stage in cross-fertilized HA embryos from mating of N2 males with HA hermaphrodites or from mating of HA males with HA hermaphrodites (fig. S6G, mating 1-3). Likewise, loss of paternal CPS-6 significantly delayed elimination of Bristol paternal mitochondria in cross-fertilized HA embryos or cross-fertilized N2 embryos (fig. S6G, mating 4, 5), when *cps-6(tm3222)* Bristol males were mated with HA hermaphrodites or N2 hermaphrodites. Although N2, *cps-6(tm3222)* Bristol, and HA hermaphrodites showed comparable levels of embryonic lethality (Fig. 4D, assays 1-3), delayed removal of wild-type Bristol paternal mitochondria in HA embryos derived from mating of HA hermaphrodites with *cps-6(tm3222)* Bristol males resulted in a significantly higher percentage of embryonic lethality than that observed in HA embryos from mating of N2 males with HA hermaphrodites (Fig. 4D, assays 4, 5, and fig. S6G, mating 2, 4). These results indicate that delayed clearance of wild-type paternal mitochondria that are slightly different from maternal mitochondria also compromises the development of the animals and that transmission of

paternal mitochondria among different wild-type variants in the same species is evolutionarily disadvantageous.

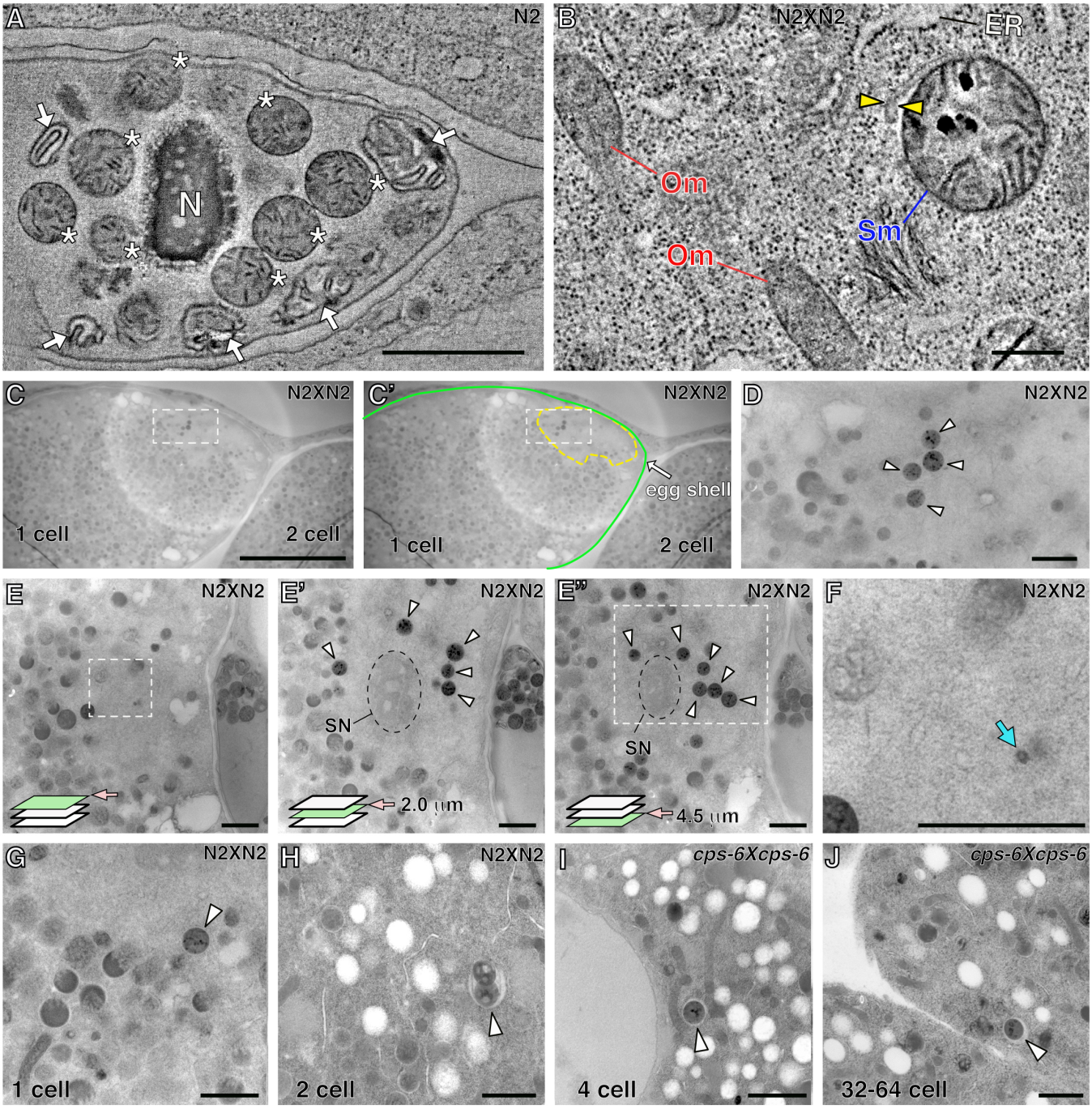

Fig. S1. Electron micrographs of paternal mitochondria in cross-fertilized N2 and *cps-6(tm3222)* embryos. (**A**) An electron tomographic slice image of a wild-type (N2) spermatozoon showing the nucleus (N), mitochondria (asterisks), and membranous organelles (arrows). (**B**) An electron tomographic slice image of a sperm mitochondrion (Sm) in an N2 zygote. Arrowheads denote limiting double membranes of an autophagosome being assembled around the sperm mitochondrion. Maternal mitochondria from the oocyte (Om) and endoplasmic reticulum (ER) are easily recognized in the image. Scale bars in A and B indicate 1 μm and 300 nm, respectively. (**C**) An electron micrograph showing a 1-cell stage

N2 embryo and a 2-cell stage N2 embryo. In the upper right corner of the 1-cell stage embryo, cytosolic particles of the oocyte appear to have been pushed in by sperm fertilization (outlined with a yellow dashed line in C'). Scale bar in C: 10 μm. (**D**) A close-up view of the cytoplasm in the 1-cell stage embryo marked with a dashed rectangle in C and C'. A cluster of paternal mitochondria with small aggregates (arrowheads) are seen, indicating that paternal mitochondria incurred internal damages as soon as they entered into the oocyte. (**E** and **F**) Three sequential electron micrographs covering the sperm entry site showing a sperm nucleus (SN), centrioles, and paternal mitochondria with small aggregates (arrowheads). Panels E' and E'' are micrographs from sections acquired at 2.0 μm and 4.5 μm underneath the section in E. F is a high magnification view of the area highlighted by a dashed rectangle in E. Centrioles contributed by the sperm are marked with an arrow in F. Given that the sperm nucleus, centrioles, and mitochondria had not been dispersed, this oocyte had been fertilized only for a few minutes. (**G** and **H**) Cross-fertilized N2 embryos at the 1-cell stage and the 2-cell stage, respectively. Two ghost paternal mitochondria were enclosed in an autophagosome in H **(**arrowhead**)**. (**I** and **J**) Cross-fertilized *cps-6(tm3222)* embryos at the 4-cell stage and the 32-64 cell stage, respectively. Degradation of the paternal mitochondria, which contained aggregates, was delayed in the mutant embryos (arrow heads). Scale bars in D to J: 1 μm.

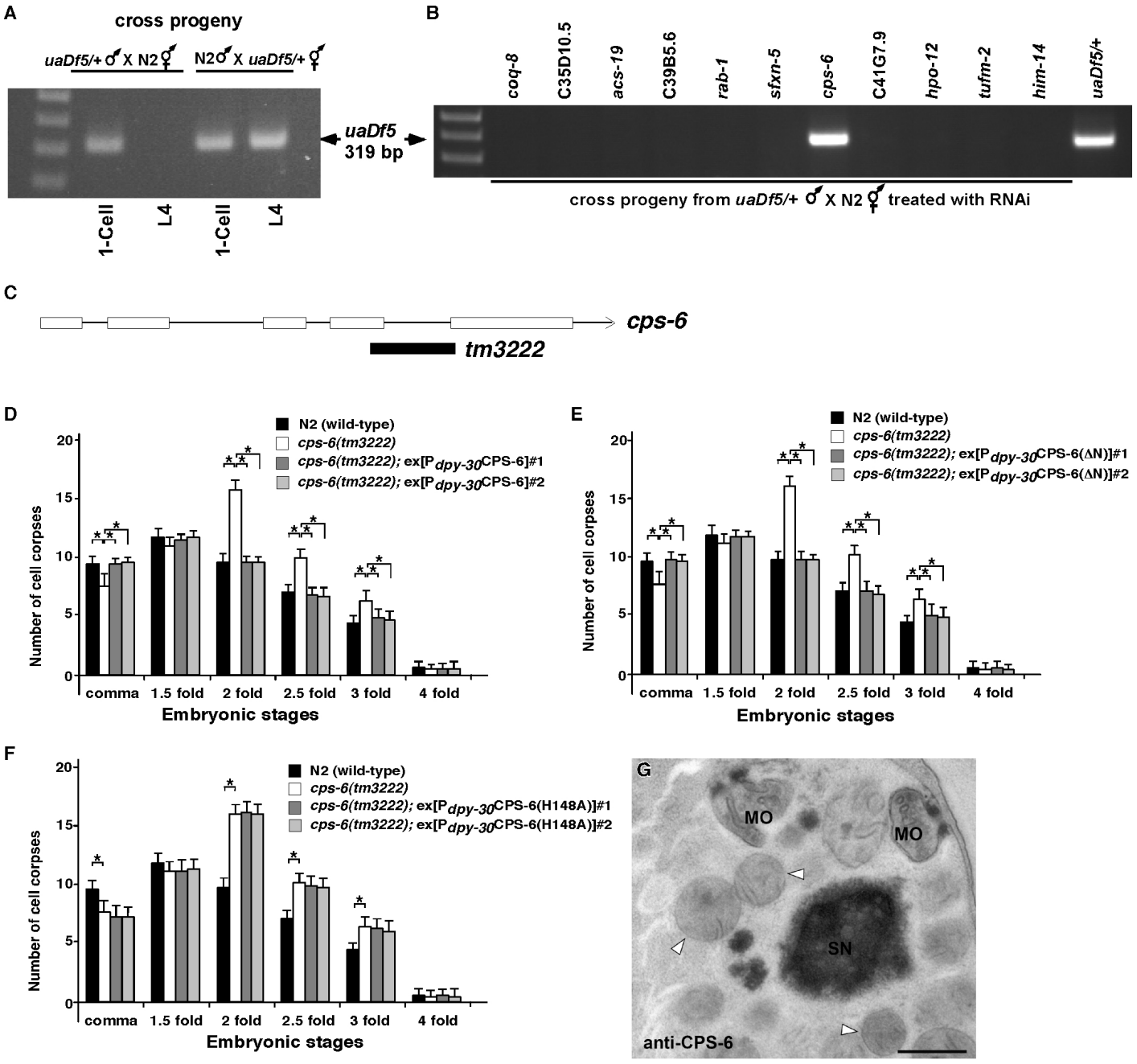

Fig. S2. Identification of *cps-6* as a gene important for paternal mitochondrial elimination (PME) by RNAi and cell death assays for the indicated *cps-6* transgenes. (**A**) PME is conserved in *C. elegans*. A single cross-fertilized 1-cell stage embryo or L4 larva derived from mating of *smIs42; uaDf5/+* males with wild-type N2 hermaphrodites or from mating of *smIs42* males with *uaDf5/+* hermaphrodites was analyzed by PCR for the presence of *uaDf5* mtDNA. *smIs42* is an integrated $P_{sur\text{-}5}$*sur-5::gfp* transgene that directs GFP expression in many cells at most developmental stages (*37*) and was used to track cross progeny. MitoTracker Red (MTR) was also used to stain males before mating to facilitate isolation of the zygotes. The expected PCR product (3861 bp) from wild-type mtDNA was not

detected under the PCR conditions used. (**B**) A candidate RNAi screen identified *cps-6* as a mitochondrion-specific gene involved in paternal mtDNA elimination. A representative PCR screen is shown, in which RNAi of *cps-6* led to persistence of *uaDf5* paternal mtDNA in 4-fold cross-fertilized embryos from mating of *smIs42; uaDf5/*+ males with N2 hermaphrodites. RNAi treatment of the other nine genes predicted to encode mitochondrial proteins did not produce detectable *uaDf5*-specific product. *him-14* was used as an RNAi control to demonstrate that the bacterial feeding protocol of RNAi worked well, because an increased frequency of males were produced. See table S1 for the list of nuclear genes screened that encode mitochondrial proteins and Materials and Methods for details of conducting this RNAi screen. (**C**) The *cps-6* gene structure and the *tm3222* deletion mutation. Exons are shown as boxes and introns as lines. The filled box indicates the region of *cps-6* removed by *tm3222*. (**D** to **F**) Rescue of the cell death defect in the *cps-6(tm3222)* mutant by the indicated *cps-6* transgenes. In the *cps-6(tm3222)* mutant, compared with N2 animals, some of the early embryonic cell deaths were delayed until the mid- or late embryonic stages (2-fold, 2.5-fold and 3-fold stages), resulting in the peak of embryonic cell deaths at the 2-fold embryonic stage and a delay-of-cell-death phenotype (8). Cell corpses were scored in the following animals: N2, *cps-6(tm3222),* and *cps-6(tm3222);* ex[P_{dpy-30}CPS-6] arrays #1-2 (D), *cps-6(tm3222);* ex[P_{dpy-30}CPS-6(ΔN)] arrays #1-2 (E), or *cps-6(tm3222);* ex[P_{dpy-30}CPS-6(H148A)] arrays #1-2 (F). Fifteen embryos were examined at each stage. The y axis represents the average number of cell corpses and error bars represent standard deviation (SD). The significance of differences between different genetic backgrounds was determined by two-way ANOVA, followed by Bonferroni comparison. *, $P < 0.001$. All other points had P values > 0.05. (**G**) An immuno-EM micrograph showing a *cps-6(tm3222)* spermatozoon. The section was labeled with the CPS-6 antibody. No immunogold particles were detected in mitochondria (arrowheads). SN: Sperm nucleus. MO: membranous organelle. The scale bar indicates 500 nm.

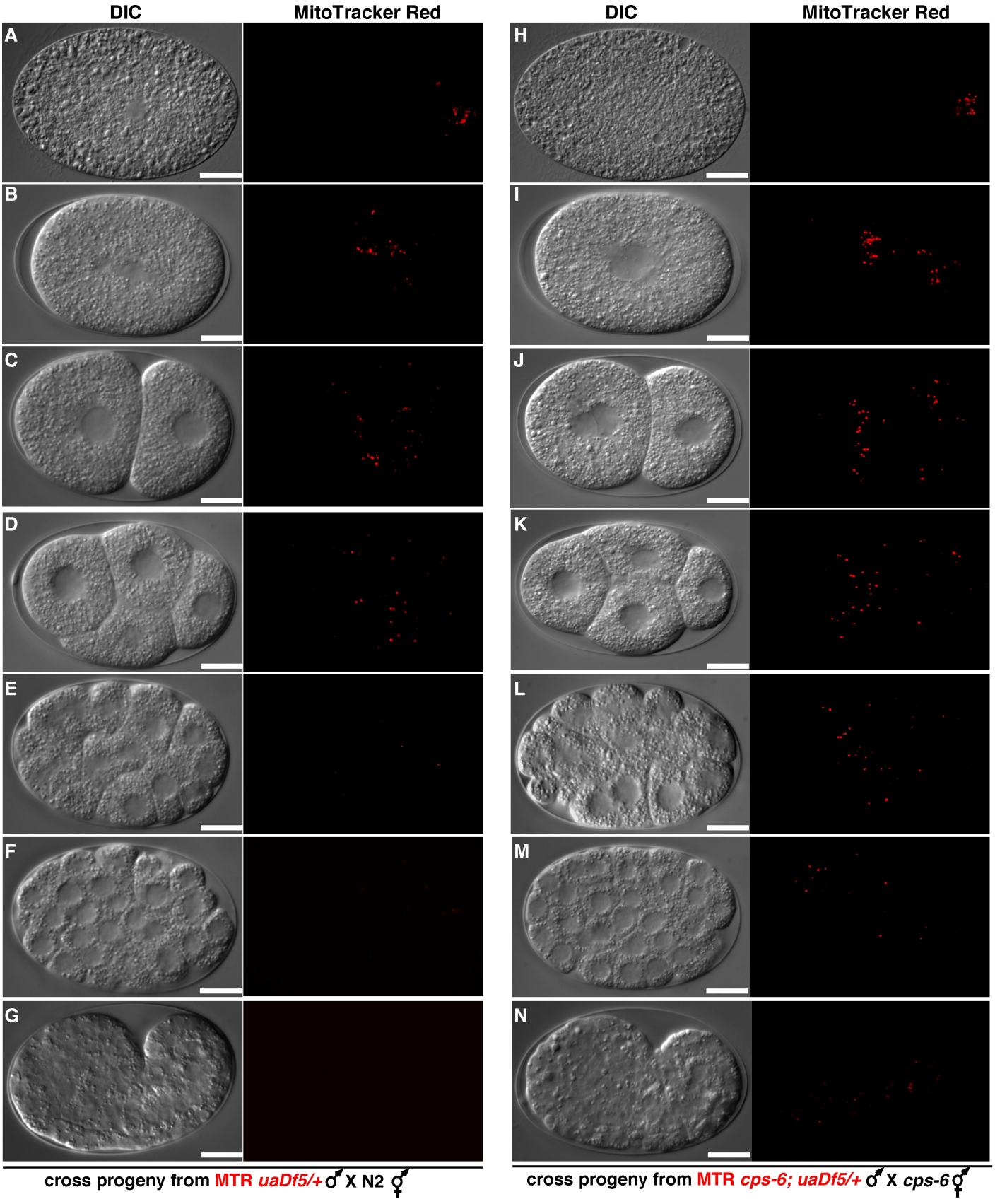
DIC
MitoTracker Red
A
B
C
D
E
F
G
cross progeny from MTR uaDf5/+ ♂ X N2 ♀
DIC
MitoTracker Red
H
I
J
K
L
M
N
cross progeny from MTR cps-6; uaDf5/+ ♂ X cps-6 ♀

Fig. S3. Inactivation of *cps-6* delays PME in *C. elegans.* (**A** to **N**) MTR-stained *uaDf5/+* males (A to G) or *cps-6(tm3222); uaDf5/+* males (H to N) were mated with unstained N2 hermaphrodites or *cps-6(tm3222)* hermaphrodites, respectively. Cross-fertilized embryos were dissected from mated hermaphrodites. Differential interference contrast (DIC) and MTR images of the embryos are shown. The red dots are paternal mitochondrial clusters stained by MTR. The stages of the embryos examined are: A zygote right after sperm entry (A and H), 1-cell stage (B and I), 2-cell stage (C and J), 4-cell stage (D and K), 32-cell stage (E and L), 64-cell stage (F and M), and comma stage embryos (approximately 550-cell stage; G and N). Scale bars represent 10 μm.

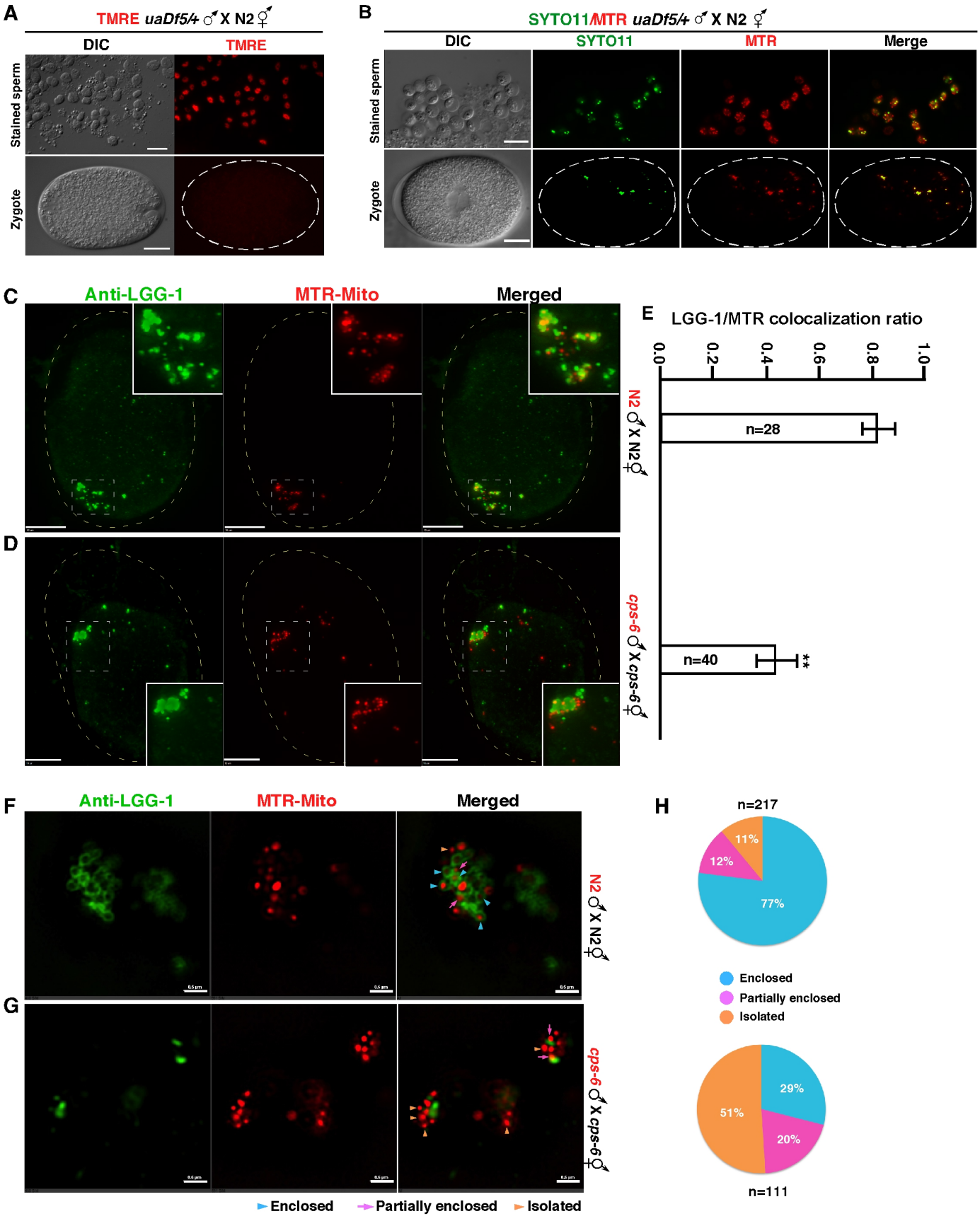
A
TMRE uaDf5/+ ♂ X N2 ♀
DIC
TMRE
Stained sperm
Zygote
B
SYTO11/MTR uaDf5/+ ♂ X N2 ♀
DIC
SYTO11
MTR
Merge
Stained sperm
Zygote
C
Anti-LGG-1
MTR-Mito
Merged
D
E
LGG-1/MTR colocalization ratio
0.0
0.2
0.4
0.6
0.8
1.0
N2 ♂ X N2 ♀
n=28
cps-6 ♂ X cps-6 ♀
n=40
**
F
Anti-LGG-1
MTR-Mito
Merged
N2 ♂ X N2 ♀
G
cps-6 ♂ X cps-6 ♀
Enclosed
Partially enclosed
Isolated
H
n=217
11%
12%
77%
Enclosed
Partially enclosed
Isolated
29%
51%
20%
n=111

Fig. S4. Depolarization of paternal mitochondria following fertilization and reduced autophagosome formation on paternal mitochondria in *cps-6(tm3222)* zygotes. (**A, B**) DIC and fluorescence images of spermatozoa stained with the indicated dyes (upper panels in A and B) and corresponding images of zygotes from the indicated crosses are shown. TMRE stained specifically spermatozoa (A). SYTO11, a nucleic acid dye, also stained specifically sperm mitochondria, because its staining patterns completely overlapped with those of MTR in both spermatozoa and the zygote (B), but appeared to only stain limited areas of sperm mitochondria, and most likely, sperm mtDNA. Notably, SYTO11 did not stain sperm nuclear DNA (B). The presence of *uaDf5* paternal mtDNA in the zygote following fertilization (A) was confirmed by PCR analysis after recovery of the imaged zygote from the agar pad. (**C, D**) Zygotes from mating of MTR-stained males with unstained hermaphrodites of the indicated genotypes were labeled with a monoclonal antibody to LGG-1 *(33)*. Images shown are anti-LGG-1 staining (Green), MTR-stained paternal mitochondria (Red), and anti-LGG-1/MTR merged images. Images were acquired using a Zeiss Axioplan 2 microscope. The *cps-6(tm3222)* allele was used. Dash rectangles highlight the areas enlarged and shown in insets. Scale bars represent 10 μm. (**E**) Quantification of the colocalization ratio of MTR-stained paternal mitochondrial clusters with LGG-1-stained autophagosomes shown in C and D. Error bars are SEM. n indicates the number of zygotes scored. The significance of difference between results from two different mating experiments was determined by unpaired Student's *t*-test. ** $P < 0.001$. (**F** and **G**) Enlarged images of Fig. 3D (F) and Fig. 3F (G), respectively, in which examples of three different categories of mitochondria are shown. MTR-stained paternal mitochondria fully enclosed by the LGG-1 autophagosomes are indicated with blue arrowheads, paternal mitochondria partially enclosed by autophagosomes are indicated with pink arrows, and paternal mitochondria away from autophagosomes (isolated) are indicated by orange arrowheads. Scale bars represent 0.5 μm. (**H**) Quantification of three types of paternal mitochondria, fully enclosed, partially enclosed, and not enclosed (Isolated) by the LGG-1 autophagosomes.

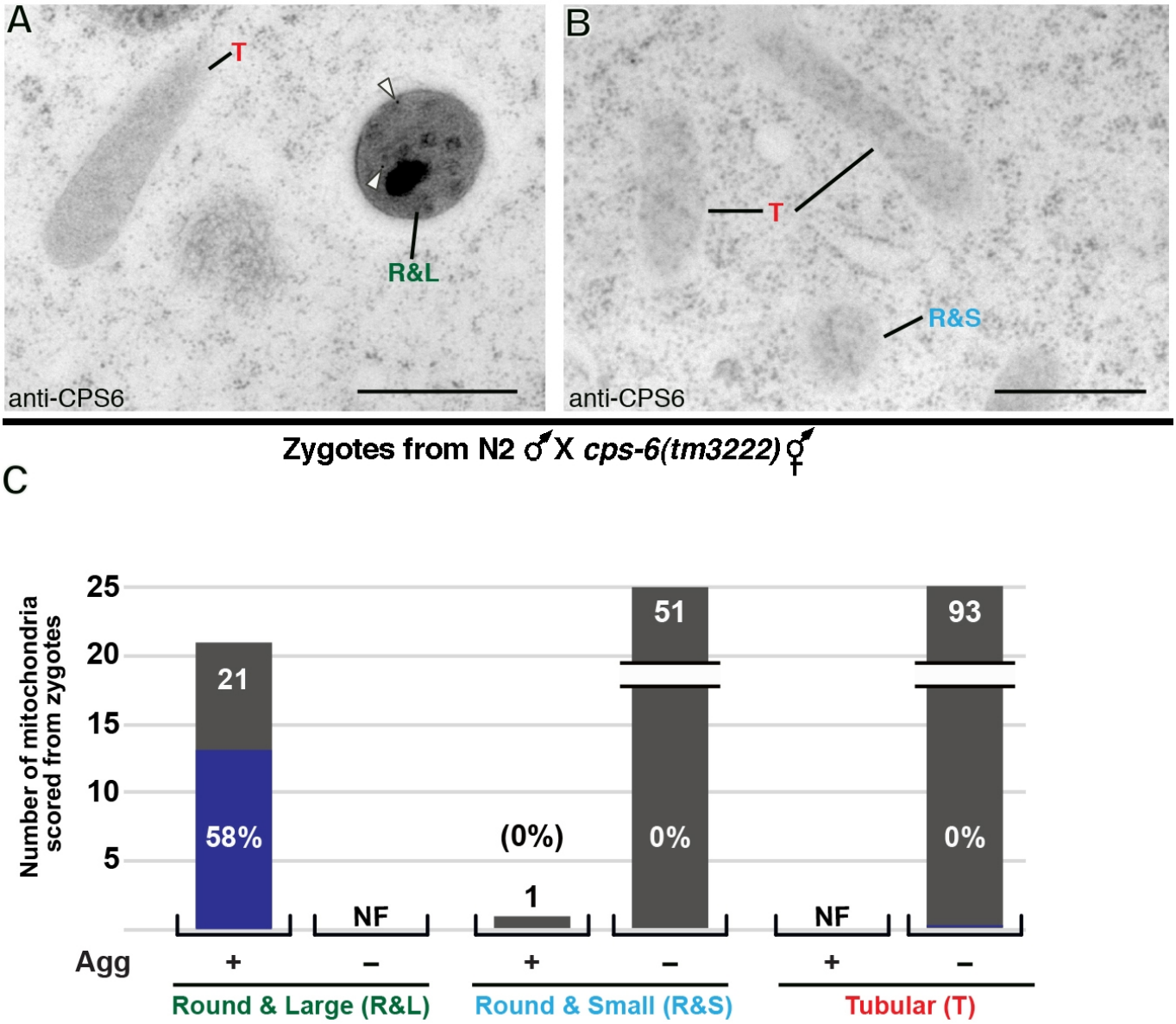

Fig. S5. Immuno-EM labeling confirms the identities of paternal mitochondria in zygotes. (**A** and **B**) Transmission electron micrographs illustrating different classes of mitochondria observed in zygotes from mating between N2 males and *cps-6(tm3222)* hermaphrodites. They are named tubular (T), round & large (R&L, diameters larger than 350 nm), and round & small (R&S, diameters smaller than 300 nm) mitochondria, respectively. Round & large mitochondria always have dark aggregates (A). CPS-6-specific immunogold particles are marked with arrowheads in A. Scale bars indicate 500 nm. (**C**) Histogram showing the numbers of different types of mitochondria scored in zygotes. Percentages of mitochondria labeled by CPS-6-specific immunogold particles are indicated in each column. Since zygotes were derived from the *cps-6(tm3222)* oocytes fertilized by N2 sperms, only sperm-originated mitochondrial CPS-6 was detected by immunogold labeling. CPS-6-specific

immunogold particles are exclusively detected in round & large mitochondria with dark aggregates (Agg) whose morphological features match completely with those of paternal mitochondria observed in zygotes (Fig. 1 and Fig. S1). In immunogold labeling experiments, antibodies cannot penetrate into plastic sections. Labeling efficiency of Round & Large mitochondria with aggregates by the CPS-6 antibody is 58% because detection by the antibody is limited to its epitope (CPS-6) exposed on the section surface. Dark aggregates and CPS-6-specific immunogold particles are not observed in tubular (T) and round & small mitochondria. Furthermore, diameters of round & small mitochondria match the thicknesses of tubular mitochondria, indicating that the former correspond to cross-sections of tubular mitochondria. These results confirm that round & large mitochondria with aggregates are paternal mitochondria while the other two types are maternal mitochondria. NF: not found.

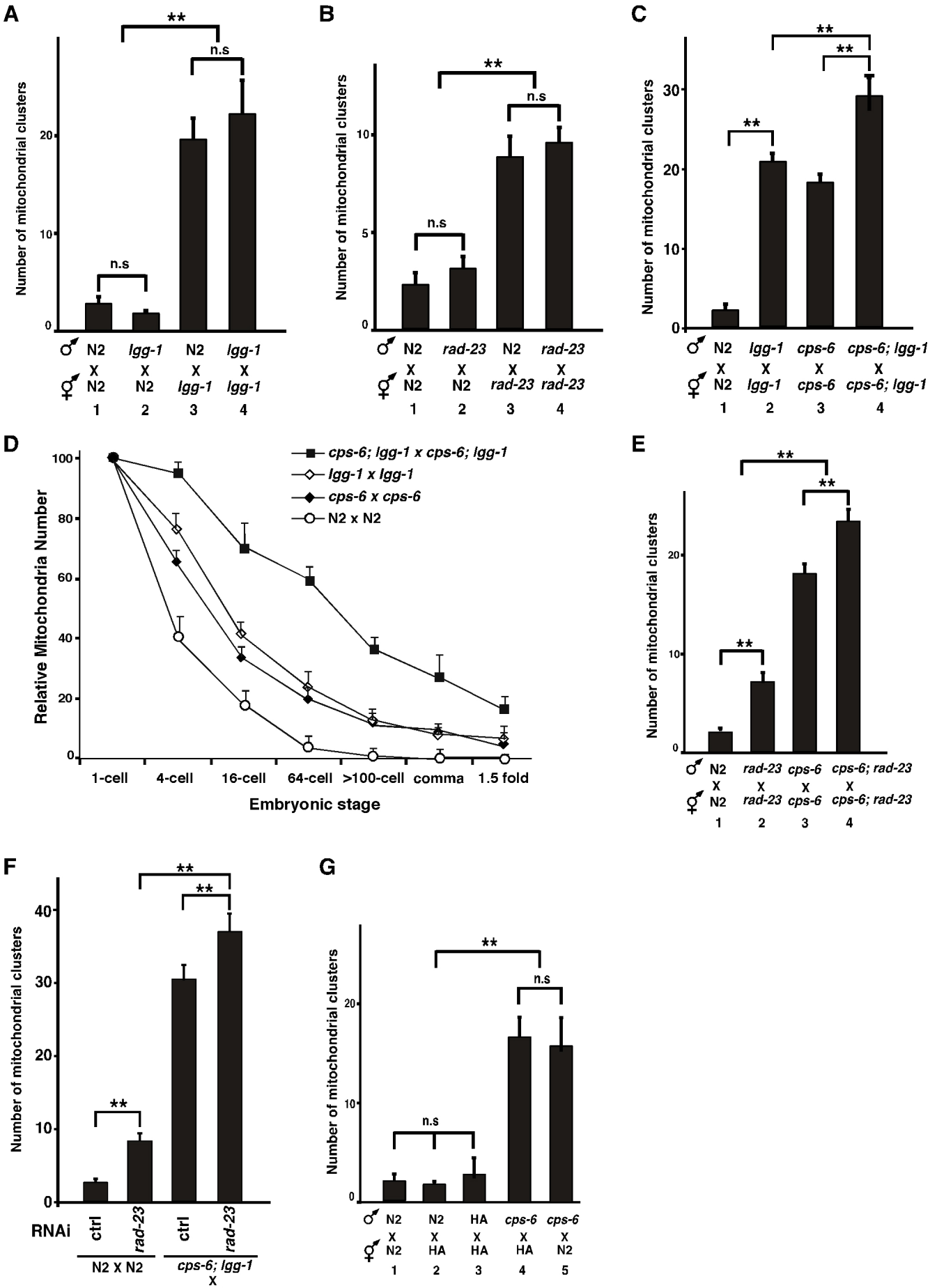
A
B
C
D
E
F
G
Number of mitochondrial clusters
n.s
**
♂ N2 lgg-1 N2 lgg-1
X X X X
♀ N2 N2 lgg-1 lgg-1
1 2 3 4
♂ N2 rad-23 N2 rad-23
X X X X
♀ N2 N2 rad-23 rad-23
1 2 3 4
♂ N2 lgg-1 cps-6 cps-6; lgg-1
X X X X
♀ N2 lgg-1 cps-6 cps-6; lgg-1
1 2 3 4
Relative Mitochondria Number
cps-6; lgg-1 x cps-6; lgg-1
lgg-1 x lgg-1
cps-6 x cps-6
N2 x N2
1-cell 4-cell 16-cell 64-cell >100-cell comma 1.5 fold
Embryonic stage
♂ N2 rad-23 cps-6 cps-6; rad-23
X X X X
♀ N2 rad-23 cps-6 cps-6; rad-23
1 2 3 4
RNAi ctrl rad-23 ctrl rad-23
N2 X N2
cps-6; lgg-1
X
cps-6; lgg-1
♂ N2 N2 HA cps-6 cps-6
X X X X X
♀ N2 HA HA HA N2
1 2 3 4 5

Fig. S6. Paternal CPS-6 acts in parallel to the maternal autophagy and proteasome pathways to promote PME. (**A** to **C, E** to **G**) Quantification of MTR-stained paternal mitochondrial clusters in 64-cell stage embryos derived from mating of males and hermaphrodites with the indicated genotypes. *lgg-1(bp500)*, *rad-23(tm2595)* and *cps-6(tm3222)* alleles were used in these experiments. HA: wild-type *C. elegans* Hawaii strain. MTR staining of males, mating with unstained hermaphrodites, and quantification of MTR-stained mitochondrial clusters were performed as described in Fig. 2D. *n*=20 for each experiment. The significance of differences between results from different experiments was determined by unpaired *t*-test, ** $P < 0.005$, "n.s" indicates no significant difference. In **F**, males and hermaphrodites were treated with control RNAi (Ctrl) or *rad-23* RNAi during mating, because the *cps-6(tm3222); lgg-1(bp500) rad-23(tm2595)* mutant is sick. (**D**) Quantification of relative paternal mitochondrial numbers in cross-fertilized embryos from the indicated mating. The numbers of MTR-stained paternal mitochondrial clusters were scored from deconvolved images of the dividing embryo at different embryonic stages. The relative paternal mitochondrial number in each zygote right after fertilization was set artificially at 100. Relative paternal mitochondrial numbers in other embryonic stages of the same embryo were normalized with the number from the zygote. Three embryos were scored for each mating experiment. *cps-6(tm3222)* and *lgg-1(bp500)* alleles were used. Error bars indicate SEM.

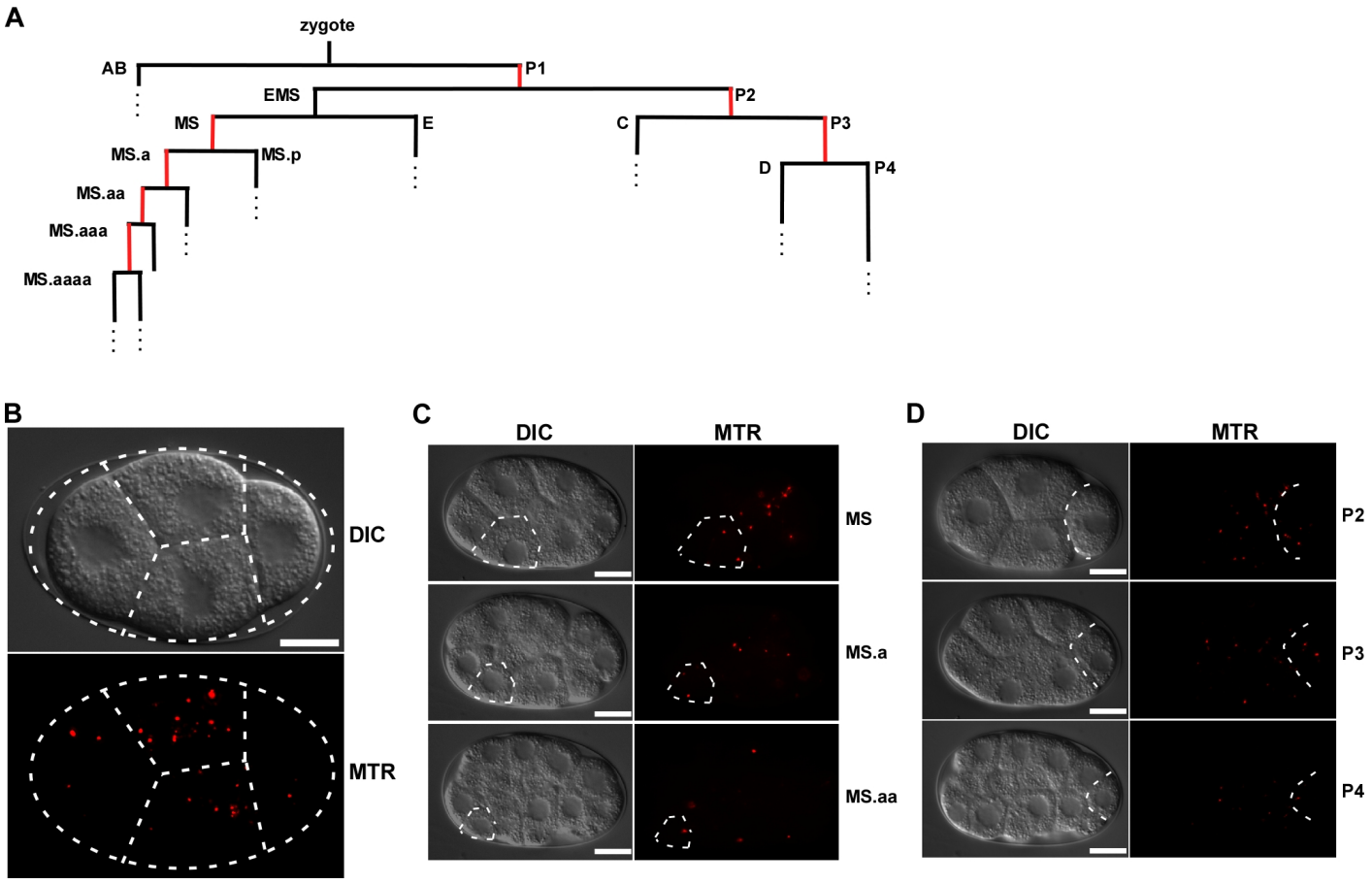

Fig. S7. Persistence of *uaDf5* paternal mitochondria in the MS and the P cell lineage of *C. elegans* embryos. (**A**) Partial lineage of *C. elegans* embryos. The horizontal axes represent the direction of cell division. The anterior daughter cell (.a) is shown at the left and the posterior daughter cell (.p) is shown at the right. The MS to MS.aaaa and the P1 to P4 cell divisions are highlighted in red. (**B**) Representative DIC and MTR images of a 4-cell stage embryo derived from mating of MTR-stained *cps-6(tm3222)*; *uaDf5/+* males with unstained *cps-6(tm3222)* hermaphrodites. MTR-stained paternal mitochondria were observed in all four blastomeres. (**C** and **D**) DIC and MTR images of a cross-fertilized embryo from mating of MTR-stained *cps-6(tm3222)*; *uaDf5/+* males with unstained *cps-6(tm3222)* hermaphrodites. MTR-stained paternal mitochondria were observed in three descendants of the MS lineage (C) and three descendants of the P lineage (D) indicated by the white dash lines. Scale bars represent 10 μm.

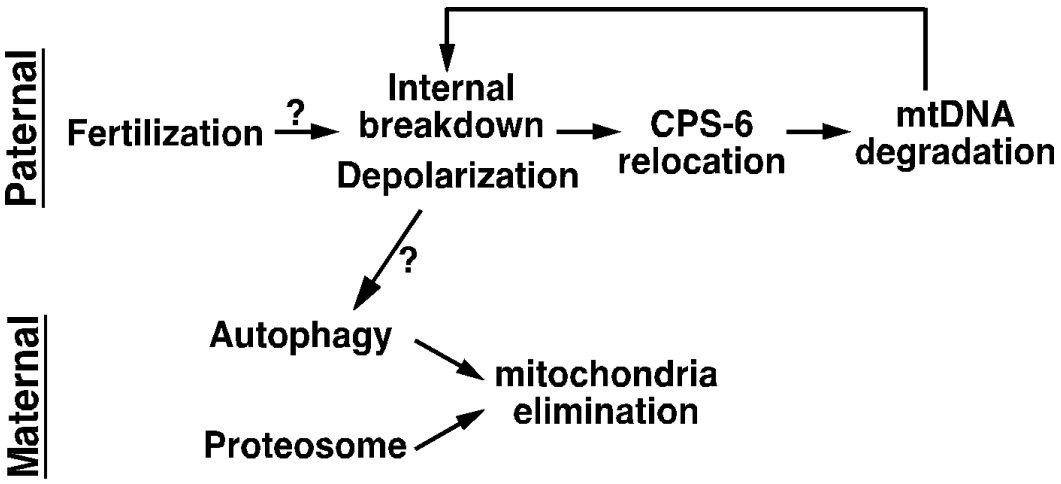

Fig. S8. A model of CPS-6-mediated paternal mitochondrial elimination. Immediately after fertilization, paternal mitochondria are depolarized and lose their inner membrane integrity, which help mark paternal mitochondria, not maternal mitochondria, for autophagy degradation. The inner membrane breakdown triggers the entry of CPS-6 from the intermembrane space of paternal mitochondria into the matrix to degrade mtDNA, which are essential for normal functions and maintenance of mitochondria. The degradation of mtDNA is detrimental and accelerates internal breakdown of paternal mitochondria, and probably, externalization of signals recognized by the maternal autophagy or proteasome machinery, leading to swift and efficient PME.

Table S1. Candidate genes predicted to encode mitochondrial proteins in *C. elegans.*

217 genes were identified as candidates that encode mitochondrial proteins (see Materials and methods) and were subjected to the RNAi screen to identify mitochondria-specific genes important for PME. Human homologues of these candidate genes are indicated.

	Sequence	Name	Human Homologue
1	B0024.9	trx-2	cDNA FLJ55158, highly similar to Thioredoxin, mitochondrial
2	B0205.6	B0205.6	Isoform Mitochondrial of Cysteine desulfurase, mitochondrial
3	B0303.3	B0303.3	cDNA FLJ56214, highly similar to Trifunctional enzyme subunit beta, mitochondrial
4	B0334.4	B0334.4	Uncharacterized protein
5	B0334.5	B0334.5	Isoform 1 of UPF0551 protein C8orf38, mitochondrial
6	B0336.4a	rgs-5	A-kinase anchor protein 10, mitochondrial
7	B0361.5	psd-1	Isoform 1 of Phosphatidylserine decarboxylase proenzyme
8	B0432.2	djr-1.1	Protein DJ-1
9	B0432.4	misc-1	Mitochondrial 2-oxoglutarate/malate carrier protein
10	B0432.8	B0432.8	Isoform 1 of Putative deoxyribonuclease TATDN3
11	C01F1.2	sco-1	Protein SCO1 homolog, mitochondrial
12	C01G10.7	C01G10.7	Isoform 1 of Citrate lyase subunit beta-like protein, mitochondrial
13	C02F5.3	C02F5.3	Developmentally-regulated GTP-binding protein 2
14	C04E6.11	C04E6.11	Uncharacterized protein
15	C06G3.11	tin-9.1	Mitochondrial import inner membrane translocase subunit Tim9
16	C08A9.1	sod-3	superoxide dismutase [Mn], mitochondrial isoform A precursor
17	C08B6.8	C08B6.8	Isoform 1 of Oligoribonuclease, mitochondrial (Fragment)
18	C08F8.2b	C08F8.2	ATP-dependent RNA helicase SUPV3L1, mitochondrial
19	C09B8.7c	pak-1	Isoform 1 of Serine/threonine-protein kinase PAK 1
20	C10G11.5	pnk-1	cDNA FLJ56439, highly similar to Pantothenate kinase 4
21	C13B9.2	C13B9.2	Isoform 1 of Glycerate kinase
22	C14A4.2	dap-3	28S ribosomal protein S29, mitochondrial isoform 2
23	C16C10.1	C16C10.1	Solute carrier family 25 member 40
24	C16C10.11	har-1	Coiled-coil-helix-coiled-coil-helix domain-containing protein 10, mitochondrial
25	C18E3.5	C18E3.5	U5 small nuclear ribonucleoprotein 40 kDa protein
26	C18E9.6	tomm-40	Isoform 1 of Mitochondrial import receptor subunit TOM40 homolog
27	C23G10.2b	C23G10.2	Ribonuclease UK114
28	C24G6.8	C24G6.8	cDNA FLJ32471 fis, clone SKNMC2000322, highly similar to Peptidyl-tRNA hydrolase 2, mitochondrial
29	C26E6.12	C26E6.12	Isoform 1 of GTP-binding protein 10
30	C29E4.10	C29E4.10	Isoform 1 of Galactocerebrosidase
31	C29F3.1	ech-1	Trifunctional enzyme subunit alpha, mitochondrial
32	C30F12.2	C30F12.2	Lactation elevated protein 1
33	C30F12.7	idhg-2	Isocitrate dehydrogenase [NAD] subunit gamma, mitochondrial
34	C31E10.7	cytb-5.1	Isoform 1 of Cytochrome b5
35	C33A12.7	ethe-1	Protein ETHE1, mitochondrial
36	C33H5.19	tag-321	Transmembrane protein 65
37	C34B2.6	C34B2.6	Lon protease homolog
38	C34C12.8	C34C12.8	GrpE protein homolog 1, mitochondrial
39	C34E10.1	gop-3	Sorting and assembly machinery component 50 homolog
40	C34G6.4	pgp-2	Multidrug resistance protein 1
41	C35D10.4	coq-8	Isoform 3 of Chaperone activity of bc1 complex-like, mitochondrial
42	C35D10.5	C35D10.5	ubiquinol-cytochrome c reductase complex chaperone CBP3 homolog isoform c
43	C36A4.9	acs-19	acetyl-coenzyme A synthetase, cytoplasmic isoform 2
44	C39B5.6	C39B5.6	Probable glutamyl-tRNA(Gln) amidotransferase subunit B, mitochondrial
45	C39F7.4	rab-1	Isoform 1 of Ras-related protein Rab-1A
46	C41C4.10	sfxn-5	Sideroflexin-5
47	C41D11.8	cps-6	Endonuclease G, mitochondrial
48	C41G7.9	C41G7.9	Translocator protein
49	C42C1.10a	hpo-12	Mitochondrial thiamine pyrophosphate carrier
50	C43E11.4	tufm-2	elongation factor Tu, mitochondrial precursor
51	C43E11.7	ndx-7	Nucleoside diphosphate-linked moiety X motif 19, mitochondrial
52	C44B7.9	pmp-2	cDNA FLJ53353, highly similar to ATP-binding cassette sub-family D member 3
53	C45B11.1	pak-2	Isoform 1 of Serine/threonine-protein kinase PAK 4
54	C47E8.5	daf-21	Heat shock protein HSP 90-beta
55	C47G2.3	C47G2.3	Mitochondrial import inner membrane translocase subunit Tim22
56	C48D1.2	ced-3	Isoform 1 of Caspase-2
57	C49G7.11	djr-1.2	Protein DJ-1
58	C50F4.12	C50F4.12	Isoform 1 of mTERF domain-containing protein 1, mitochondrial
59	C50H11.1	acs-21	Isoform 1 of Acyl-CoA synthetase family member 3, mitochondrial
60	C52E12.2	unc-104	KIF1A variant protein
61	C54G10.4	C54G10.4	Mitochondrial carnitine/acylcarnitine carrier protein CACL
62	C54G4.8	cyc-1	Cytochrome c1, heme protein, mitochondrial
63	C56A3.6	C56A3.6	EF-hand domain-containing family member A2
64	C56G2.1	C56G2.1	Isoform 1 of A-kinase anchor protein 1, mitochondrial
65	D1037.3	ftn-2	Ferritin heavy chain
66	D1037.4	rab-8	Ras-related protein Rab-8B
67	D1046.3	D1046.3	S-adenosylmethionine mitochondrial carrier protein isoform a
68	D1054.15	tag-135	Isoform 2 of Pleiotropic regulator 1
69	D2013.5	eat-3	dynamin-like 120 kDa protein, mitochondrial isoform 8
70	D2023.6	D2023.6	Isoform 2 of Uncharacterized aarF domain-containing protein kinase 1

71	D2030.2	D2030.2	ATP-dependent Clp protease ATP-binding subunit clpX-like, mitochondrial
72	DH11.1	glna-2	Isoform 1 of Glutaminase kidney isoform, mitochondrial
73	DY3.1	tin-13	Mitochondrial import inner membrane translocase subunit Tim13
74	E04A4.4	hoe-1	Isoform 1 of Zinc phosphodiesterase ELAC protein 2
75	E04A4.5	E04A4.5	Mitochondrial import inner membrane translocase subunit Tim17-B
76	E04F6.2	E04F6.2	Isoform 2 of Parkin coregulated gene protein
77	EEED8.9	pink-1	Isoform 1 of Serine/threonine-protein kinase PINK1, mitochondrial
78	F01G4.6	F01G4.6	Isoform B of Phosphate carrier protein, mitochondrial
79	F09E5.15	prdx-2	Peroxiredoxin-2
80	F09E5.8	F09E5.8	Proline synthetase co-transcribed homolog (Bacterial), isoform CRA_b
81	F10D11.1	sod-2	superoxide dismutase [Mn], mitochondrial isoform A precursor
82	F13B9.8b	fis-2	Mitochondrial fission 1 protein
83	F13G3.7	F13G3.7	Solute carrier family 25 member 44
84	F14F4.3	mrp-5	Multidrug resistance-associated protein 5
85	F15A4.11	tag-281	Transmembrane protein C9orf46
86	F15D3.6	F15D3.6	Protein slowmo homolog 2
87	F15D3.7	F15D3.7	Mitochondrial import inner membrane translocase subunit Tim23
88	F17E5.2	F17E5.2	Isoform 2 of Calcium-binding mitochondrial carrier protein SCaMC-2
89	F20D1.9	F20D1.9	Mitochondrial glutamate carrier 2
90	F20D6.11	F20D6.11	Isoform 3 of Apoptosis-inducing factor 3
91	F21C3.3	hint-1	Histidine triad nucleotide-binding protein 1
92	F23H11.9	crls-1	Isoform 1 of Cardiolipin synthase
93	F23H12.1	snb-2	Uncharacterized protein
94	F23H12.2	tomm-20	Mitochondrial import receptor subunit TOM20 homolog
95	F25H2.5	ndk-1	Isoform 1 of Nucleoside diphosphate kinase B
96	F25H9.7	F25H9.7	Protein ACN9 homolog, mitochondrial
97	F26H11.5	exl-1	Uncharacterized protein
98	F26H9.6	rab-5	Ras-related protein Rab-5B
99	F28C10.3	F28C10.3	Ribosomal protein S6 kinase alpha-3
100	F28C6.8	F28C6.8	Isoform 1 of Protein-tyrosine phosphatase mitochondrial 1
101	F29C12.4	F29C12.4	Isoform 1 of Elongation factor G, mitochondrial
102	F29C4.6	tut-1	Cytoplasmic tRNA 2-thiolation protein 1
103	F30A10.5	stl-1	Stomatin-like protein 2
104	F31D4.3	fkb-6	Peptidyl-prolyl cis-trans isomerase FKBP4
105	F32A7.4	F32A7.4	Isoform 1 of Methyltransferase-like protein 17, mitochondrial
106	F32D1.3	F32D1.3	Transmembrane and TPR repeat-containing protein 2
107	F32H2.5	fasn-1	Fatty acid synthase
108	F33A8.6	F33A8.6	Integrin-linked kinase-associated serine/threonine phosphatase 2C
109	F36H1.2	tag-144	Uncharacterized protein
110	F38B2.1	ifa-1	Isoform C of Prelamin-A/C
111	F38B6.6	F38B6.6	Isoform 3 of Transmembrane and TPR repeat-containing protein 4
112	F39B2.11	mtx-1	Isoform 1 of Metaxin-1
113	F39B2.7	F39B2.7	Isoform 2 of tRNA modification GTPase GTPBP3, mitochondrial
114	F43G9.3	F43G9.3	Solute carrier family 25 member 42
115	F44E2.6	F44E2.6	Similar to Methionine-R-sulfoxide reductase B2, mitochondrial precursor
116	F44E7.4b	F44E7.4	Insulin-degrading enzyme
117	F44E7.9	F44E7.9	Isoform 2 of Uncharacterized protein C20orf24
118	F45G2.8	F45G2.8	Mitochondrial import inner membrane translocase subunit TIM16
119	F45G2.9	F45G2.9	Putative ribosomal RNA methyltransferase 2
120	F46B6.6a	F46B6.6	Translation initiation factor IF-2, mitochondrial
121	F46E10.1	acs-1	cDNA FLJ51819, weakly similar to Long-chain-fatty-acid--CoA ligase
122	F46G10.3	sir-2.3	NAD-dependent ADP-ribosyltransferase sirtuin-4
123	F46G10.7	sir-2.2	NAD-dependent ADP-ribosyltransferase sirtuin-4
124	F46G11.1	F46G11.1	Isoform 1 of Twinkle protein, mitochondrial
125	F46H5.3	F46H5.3	Creatine kinase M-type
126	F49E8.5	dif-1	Mitochondrial carnitine/acylcarnitine carrier protein
127	F52C9.3	F52C9.3	cDNA FLJ59963, highly similar to Homo sapiens multiple substrate lipid kinase (MULK), mRNA
128	F52F12.1	"oct-1"	Isoform 1 of Solute carrier family 22 member 5
129	F52F12.7	F52F12.7	Uncharacterized protein
130	F52H3.2	F52H3.2	Isoform 5 of Protein MTO1 homolog, mitochondrial
131	F53A3.7	F53A3.7	DNL-type zinc finger protein
132	F53F10.3	F53F10.3	Brain protein 44
133	F53F10.4	unc-108	Ras-related protein Rab-2A
134	F53G12.1	rab-11.1	cDNA FLJ61136, highly similar to Ras-related protein Rab-11A
135	F54B3.3	atad-3	Isoform 2 of ATPase family AAA domain-containing protein 3A
136	F54C9.6	bcs-1	Mitochondrial chaperone BCS1
137	F55C5.5	tsfm-1	Isoform 2 of Elongation factor Ts, mitochondrial
138	F56A11.5	F56A11.5	Isoform 1 of MOSC domain-containing protein 1, mitochondrial
139	F56B3.11a	F56B3.11	TIM21-like protein, mitochondrial
140	F56C11.3	F56C11.3	Isoform 1 of FAD-linked sulfhydryl oxidase ALR
141	F56E3.3	klp-4	Isoform 3 of Kinesin-like protein KIF13A
142	F56H1.6	rad-8	Isoform 1 of Reticulon-4-interacting protein 1, mitochondrial
143	F58G11.1	letm-1	Isoform 1 of LETM1 and EF-hand domain-containing protein 1, mitochondrial
144	F59A2.3	cri-3	Complement component 1 Q subcomponent-binding protein, mitochondrial
145	F59C6.12	F59C6.12	Isoform 1 of UPF0598 protein C8orf82
146	F59G1.7	frh-1	Isoform 1 of Frataxin, mitochondrial
147	H06I04.2	sft-1	Isoform 1 of Surfeit locus protein 1
148	H13N06.4a	suox-1	Sulfite oxidase, mitochondrial
149	H14A12.2a	fum-1	Isoform Mitochondrial of Fumarate hydratase, mitochondrial

150	H24K24.4	H24K24.4	Isoform 1 of tRNA (uracil-5-)-methyltransferase homolog A (Fragment)
151	H32C10.1	H32C10.1	Isoform 1 of Cat eye syndrome critical region protein 5
152	K01C8.7a	K01C8.7	Mitochondrial folate transporter/carrier
153	K01H12.2	ant-1.3	ADP/ATP translocase 1
154	K02B2.3	mcu-1	Isoform 3 of Calcium uniporter protein, mitochondrial
155	K02D10.1	K02D10.1	protein NipSnap homolog 1 isoform 2
156	K02F3.2	K02F3.2	Calcium-binding mitochondrial carrier protein Aralar1
157	K04D7.2	mspn-1	Isoform 1 of ATPase family AAA domain-containing protein 1
158	K05C4.7	K05C4.7	Armadillo repeat-containing protein 1
159	K07A1.12	lin-53	Isoform 2 of Histone-binding protein RBBP4
160	K07B1.3	ucp-4	Mitochondrial uncoupling protein 4
161	K08F11.5	K08F11.5	Isoform 1 of Mitochondrial Rho GTPase 1
162	K09A9.2	rab-14	Ras-related protein Rab-14
163	K09E4.3	K09E4.3	Isoform 1 of Probable methyltransferase C20orf7, mitochondrial
164	K09H11.1	K09H11.1	Isoform 1 of Acyl-CoA dehydrogenase family member 10
165	K11G12.5	K11G12.5	Isoform 1 of Mitochondrial dicarboxylate carrier
166	K11H12.1	K11H12.1	BolA-like protein 1
167	K11H12.8a	K11H12.8	cDNA FLJ59630, highly similar to Growth hormone-inducible transmembrane protein
168	K11H3.1	gpdh-2	Glycerol-3-phosphate dehydrogenase [NAD+], cytoplasmic
169	K11H3.3	K11H3.3	Tricarboxylate transport protein, mitochondrial
170	M01E5.2	M01E5.2	GTP-binding protein 5
171	M01F1.3	M01F1.3	Lipoyl synthase, mitochondrial
172	M03C11.5	ymel-1	Isoform 2 of ATP-dependent zinc metalloprotease YME1L1
173	M05B5.4	M05B5.4	Group XV phospholipase A2
174	M88.7	M88.7	CDGSH iron-sulfur domain-containing protein 3, mitochondrial
175	R02F2.9	R02F2.9	Peptidyl-tRNA hydrolase ICT1, mitochondrial
176	R05G6.7	R05G6.7	Isoform 1 of Voltage-dependent anion-selective channel protein 2
177	R06C1.2	fdps-1	farnesyl pyrophosphate synthase isoform b
178	R07B1.12	glo-1	Ras-related protein Rab-32
179	R07E5.13	R07E5.13	Brain protein 44-like protein
180	R07H5.3	nuaf-3	Isoform a of NADH dehydrogenase [ubiquinone] 1 alpha subcomplex assembly factor 3
181	R107.2	R107.2	cDNA FLJ61130
182	R10E4.5	nth-1	Endonuclease III-like protein 1
183	R10H10.1	lpd-8	Isoform 1 of NFU1 iron-sulfur cluster scaffold homolog, mitochondrial
184	R10H10.6	R10H10.6	cDNA, FLJ96841
185	R11A8.4	sir-2.1	NAD-dependent deacetylase sirtuin-1
186	R11A8.5	R11A8.5	Prostaglandin E synthase 2
187	R11D1.1	R11D1.1	Isoform 1 of DDB1- and CUL4-associated factor 5
188	R11F4.1	R11F4.1	Isoform 1 of Glycerol kinase
189	R144.13	R144.13	Coenzyme Q-binding protein COQ10 homolog B, mitochondrial
190	R151.7	R151.7	Uncharacterized protein
191	R53.5	R53.5	UPF0765 protein C10orf58
192	R74.4	dnj-16	25 kDa protein
193	T01B11.2a	T01B11.2	Isoform 1 of Alanine--glyoxylate aminotransferase 2-like 1
194	T01B11.4	ant-1.4	ADP/ATP translocase 1
195	T02D1.5	pmp-4	ATP-binding cassette sub-family D member 2
196	T03F1.7	T03F1.7	Dimethyladenosine transferase 1, mitochondrial
197	T04F8.1	sfxn-1.5	Sideroflexin-1
198	T05E11.3	T05E11.3	Endoplasmin
199	T05G5.5	T05G5.5	Isoform 1 of Dephospho-CoA kinase domain-containing protein
200	T07D4.3	rha-1	ATP-dependent RNA helicase A
201	T08B2.7	T08B2.7	Trifunctional enzyme subunit alpha, mitochondrial
202	T09B4.9	T09B4.9	Mitochondrial import inner membrane translocase subunit TIM44
203	T09F3.2	T09F3.2	Solute carrier family 25 member 33
204	T10B11.1	pcbd-1	Pterin-4-alpha-carbinolamine dehydratase
205	T10B11.2	T10B11.2	Ceramide kinase
206	T10B5.5	cct-7	T-complex protein 1 subunit eta
207	T10E9.7a	nuo-2	NADH dehydrogenase [ubiquinone] iron-sulfur protein 3, mitochondrial
208	T10F2.2	T10F2.2	Mitochondrial ornithine transporter 1
209	T10H9.4	snb-1	cDNA FLJ61298, highly similar to Vesicle-associated membrane protein 1
210	T13C5.8	mtp-18	Isoform 1 of Mitochondrial fission process protein 1
211	T14G11.3	immt-1	Uncharacterized protein
212	T18D3.9	T18D3.9	Protein Mpv17
213	T19B4.4	dnj-21	DnaJ homolog subfamily C member 15
214	T20B3.1	T20B3.1	Peroxisomal carnitine O-octanoyltransferase
215	T20D3.11	clec-30	C-type LECtin
216	T20D3.5b	T20D3.5	Mitochondrial carrier triple repeat protein 1
217	T20G5.10	T20G5.10	Isoform 1 of Biogenesis of lysosome-related organelles complex 1 subunit 1

Movie S1 legend. Tomographic volume of the area surrounded by the dash rectangle in fig. S1C''. Paternal mitochondria are indicated with arrowheads. No sign of autophagsome assembly is detected around paternal mitochondria with aggregates in their matrices.

REFERENCES AND NOTES

23. D. J. Pagliarini *et al*., A mitochondrial protein compendium elucidates complex I disease biology. *Cell* **134**, 112 (2008).
24. T. A. Rosenquist, J. Kimble, Molecular cloning and transcript analysis of fem-3, a sex-determination gene in *Caenorhabditis elegans*. *Genes Dev*. **2**, 606 (1988).
25. S. Brenner, The genetics of *Caenorhabditis elegans*. *Genetics* **77**, 71 (1974).
26. X. Wang, C. Yang, J. Chai, Y. Shi, D. Xue, Mechanisms of AIF-mediated apoptotic DNA degradation in *Caenorhabditis elegans*. *Science* **298**, 1587 (2002).
27. X. Wang *et al*., Cell Corpse Engulfment Mediated by *C. elegans* Phosphatidylserine Receptor Through CED-5 and CED-12. *Science* **302**, 1563 (2003).
28. D. G. Breckenridge, B. H. Kang, D. Xue, Bcl-2 proteins EGL-1 and CED-9 do not regulate mitochondrial fission or fusion in *Caenorhabditis elegans*. *Curr. Biol*. **19**, 768 (2009).
29. B. H. Kang, Electron microscopy and high-pressure freezing of *Arabidopsis*. *Methods Cell Biol*. **96**, 259 (2010).
30. B. H. Kang, E. Nielsen, M. L. Preuss, D. Mastronarde, L. A. Staehelin, Electron tomography of RabA4b- and PI-4Kbeta1-labeled trans Golgi network compartments in *Arabidopsis*. *Traffic* **12**, 313 (2011).
31. X. Wang *et al*., *C. elegans* mitochondrial factor WAH-1 promotes phosphatidylserine externalization in apoptotic cells through phospholipid scramblase SCRM-1. *Nat. Cell Biol*. **9**, 541 (2007).
32. D. R. Hsu, P. T. Chuang, B. J. Meyer, DPY-30, a nuclear protein essential early in embryogenesis for *Caenorhabditis elegans* dosage compensation. *Development* **121**, 3323 (1995).
33. Y. Tian *et al*., *C. elegans* screen identifies autophagy genes specific to multicellular organisms. *Cell* **141**, 1042 (2010).
34. D. C. Wallace, Why Do We Still Have a Maternally Inherited Mitochondrial DNA? Insights from Evolutionary Medicine. *Annu. Rev. Biochem*. **76**, 781 (2007).
35. M. W. Nachman, W. M. Brown, M. Stoneking, C. F. Aquadro, Nonneutral mitochondrial DNA variation in humans and chimpanzees. *Genetics* **142**, 953 (1996).
36. B. Bowerman, C. A. Shelton, Cell polarity in the early *Caenorhabditis elegans* embryo. *Curr. Opin. Genet. Dev*. **9**, 390 (1999).
37. T. Gu, S. Orita, M. Han, *Caenorhabditis elegans* SUR-5, a novel but conserved protein, negatively regulates LET-60 Ras activity during vulval induction. *Mol. Cell Biol*. **18**, 4556 (1998).